

Waterproof AlInGaP optoelectronics on stretchable substrates with applications in biomedicine and robotics

Rak-Hwan Kim^{1†}, Dae-Hyeong Kim^{1†}, Jianliang Xiao^{1,2}, Bong Hoon Kim^{1,3}, Sang-II Park¹, Bruce Panilaitis⁴, Roozbeh Ghaffari⁵, Jimin Yao⁶, Ming Li^{2,7}, Zhuangjian Liu⁸, Viktor Malyarchuk¹, Dae Gon Kim¹, An-Phong Le⁶, Ralph G. Nuzzo⁶, David L. Kaplan⁴, Fiorenzo G. Omenetto⁴, Yonggang Huang², Zhan Kang⁷ and John A. Rogers^{1*}

Inorganic light-emitting diodes and photodetectors represent important, established technologies for solid-state lighting, digital imaging and many other applications. Eliminating mechanical and geometrical design constraints imposed by the supporting semiconductor wafers can enable alternative uses in areas such as biomedicine and robotics. Here we describe systems that consist of arrays of interconnected, ultrathin inorganic light-emitting diodes and photodetectors configured in mechanically optimized layouts on unusual substrates. Light-emitting sutures, implantable sheets and illuminated plasmonic crystals that are compatible with complete immersion in biofluids illustrate the suitability of these technologies for use in biomedicine. Waterproof optical-proximity-sensor tapes capable of conformal integration on curved surfaces of gloves and thin, refractive-index monitors wrapped on tubing for intravenous delivery systems demonstrate possibilities in robotics and clinical medicine. These and related systems may create important, unconventional opportunities for optoelectronic devices.

All established forms of inorganic light-emitting diodes (LEDs) and photodetectors (PDs) incorporate rigid, flat and brittle semiconductor wafers as supporting substrates, thereby restricting the ways in which these devices can be used. Research in organic optoelectronic materials is motivated, in part, by the potential for alternative applications enabled by integration of thin-film devices on flexible sheets of plastic^{1–3}. Many impressive results have been achieved in recent years, several of which are moving toward commercialization^{4,5}. There is growing interest in the use of organic and inorganic micro/nanomaterials in similarly unusual forms on plastic^{6–9}, paper^{10–12}, textile¹³, rubber¹⁴ and other flat or curved^{15–17} substrates. We recently reported some ideas for using inorganic LEDs in ultrathin geometries separated from their growth wafers, to bridge, at least to some useful extent, the gap in capabilities between inorganic and organic LEDs while retaining certain attractive features of each¹⁸. The present paper extends these concepts into new areas and implements the results in mechanically optimized layouts to achieve arrays of inorganic LEDs and PDs in systems that can accommodate extreme modes of mechanical deformation, for integration on substrates of diverse materials and formats. Additionally, the reported materials and design strategies enable operation even on complete immersion in saline solutions, biofluids, liquids of relevance to clinical

medicine and soapy water, thereby opening new opportunities for seamless integration of optoelectronics with biomedical and robotic systems. Light-emitting sutures, thin implantable sheets (that is LED tattoos) and balloon catheters, and flexible, optical proximity and refractive-index sensors provide some examples. Specifically, this paper describes seven advances, in the following order: (1) experimental and theoretical aspects of mechanical designs that enable freely deformable, interconnected collections of LEDs and PDs on soft, elastomeric membranes, bands and coatings, (2) strategies for achieving high effective fill factors in these systems, using laminated multilayer constructs, (3) device examples on diverse substrates and in varied geometrical forms, (4) low-modulus, biocompatible encapsulation materials that preserve key mechanical properties and, at the same time, enable robust operation when integrated on or implanted in living systems, (5) stretchable optoelectronic components for biomedicine, with *in vivo* demonstrations in animal models, (6) illuminated plasmonic crystal devices, as high-performance refractive-index monitors for intravenous delivery systems and (7) waterproof optical proximity sensors that mount on the curved fingertips of vinyl gloves, for possible use in robotics or advanced surgical devices.

For active materials, we exploit thin epitaxial semiconductor layers grown on GaAs wafers, and then vertically etched to define

¹Department of Materials Science and Engineering, Beckman Institute for Advanced Science and Technology and Frederick Seitz Materials Research Laboratory, University of Illinois at Urbana-Champaign, Urbana, Illinois 61801, USA, ²Department of Mechanical Engineering and Department of Civil and Environmental Engineering, Northwestern University, Evanston, Illinois 60208, USA, ³Department of Materials Science and Engineering, Korea Advanced Institute of Science and Technology (KAIST), 373-1 Guseong-dong, Yuseong-gu, Daejeon, Republic of Korea, ⁴Department of Biomedical Engineering, Tufts University, Medford, Massachusetts 02155, USA, ⁵MC10 Inc., 36 Cameron Avenue, Cambridge, Massachusetts 02140, USA, ⁶Department of Chemistry, University of Illinois at Urbana-Champaign, Urbana, Illinois 61801, USA, ⁷State Key Laboratory of Structural Analysis for Industrial Equipment, Dalian University of Technology, Dalian 116024, China, ⁸Institute of High Performance Computing, 1 Fusionopolis Way, #16-16 Connexis, 138632, Singapore.
†These authors contributed equally to this work. *e-mail: jrogers@uiuc.edu.

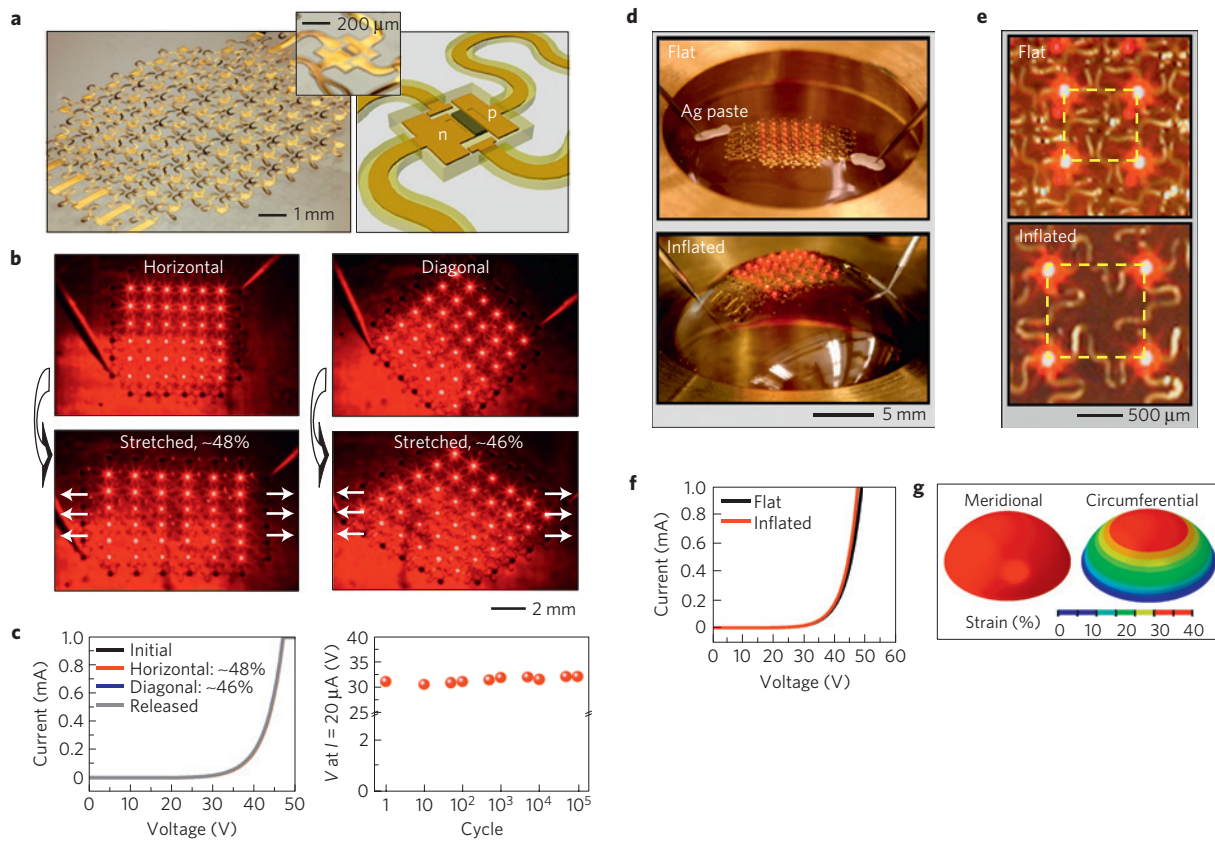


Figure 1 | Device layouts of μ -ILED arrays and their responses to uniaxial and balloon-shape biaxial stretching. **a**, Optical image of a 6×6 array of μ -ILEDs (100 $\mu\text{m} \times 100 \mu\text{m}$, and 2.5 μm thick, in an interconnected array with a pitch of $\sim 830 \mu\text{m}$) with non-coplanar serpentine bridges on a thin ($\sim 400 \mu\text{m}$) PDMS substrate (left-hand frame). Schematic illustration (right) and corresponding photograph (inset) of a representative device, with encapsulation. **b**, Optical images of a stretchable 6×6 array of μ -ILEDs, showing uniform emission characteristics under different uniaxial applied strains (top left, 0%, bottom left, 48% along horizontal direction; top right, 0%, bottom right, 46% along diagonal direction). **c**, Current-voltage (I - V) characteristics of this array measured in the strained configurations shown in **b** (left) and voltage at 20 μA current for different cycles of stretching to 75% along the horizontal direction (right). **d**, Tilted-view optical images of a stretchable array (6×6) of μ -ILEDs on a thin ($\sim 500 \mu\text{m}$) PDMS membrane in a flat configuration (top) and in a hemispherical, balloon state (bottom) induced by pneumatic pressure. **e**, Magnified view of **d** from the top. The yellow dashed boxes highlight the dimensional changes associated with the biaxial strain. **f**, I - V characteristics of the array in its flat and inflated states. **g**, Distribution of meridional and circumferential strains determined by 3D-FEM.

lateral dimensions of devices built with them. Release from the wafer through selective elimination of an underlying layer of AlAs, followed by transfer printing, accomplishes integration on substrates of interest, according to previously reported procedures¹⁸. The fabrication scheme described here uses a dual-transfer process that involves first printing the semiconductor materials onto a temporary substrate (glass plate coated with a trilayer of epoxy–polyimide–poly(methylmethacrylate) (PMMA)) to form contacts, interconnections and structural bridges, and encapsulation layers. Dissolving the PMMA releases fully formed, interconnected collections of devices. A second transfer-printing step achieves integration on elastomeric sheets (for example, poly(dimethylsiloxane) (PDMS)) or other substrates coated with thin layers of PDMS, with strong bonding only at the locations of the devices. For all examples described in the following, the LEDs (to which we refer as μ -ILEDs to highlight the small sizes and the distinction over organic devices, as per our previous report¹⁸) and the PDs (that is, μ -IPDs) have lateral dimensions of $100 \times 100 \mu\text{m}$ and thicknesses of 2.5 μm , corresponding to volumes that are orders of magnitude smaller than those of commercially available devices¹⁹. The thin geometries are critically important because they enable the use of thin-film metallization for interconnect and optimized mechanical designs, described next. Details of the processing and layouts appear in Supplementary Figs S1–S3.

Figure 1a and Supplementary Fig. S4 present optical images, schematic illustrations, scanning electron microscope images and finite-element modelling of the mechanics of arrays of μ -ILEDs connected by serpentine-shaped ribbons that serve as either structural bridges or electrical interconnects, transferred to a thin, prestrained sheet of PDMS ($\sim 400 \mu\text{m}$ thick). Here, and in other examples described next, the devices are connected in series (Supplementary Fig. S2a), such that all of them turn on and off simultaneously; a single failed device leads to failure of the entire array. The interconnects consist of thin films of metal with photodefined layers of epoxy on the top and bottom to locate the metal at the neutral mechanical plane. The bridges are similar, but without the metal. Detailed geometries appear in Supplementary Fig. S3. Releasing the prestrain yields non-coplanar layouts in the serpentines through a controlled, nonlinear buckling response, as shown in the left-hand frame of Fig. 1a ($\sim 20\%$ prestrain). The right-hand frame and inset of Fig. 1a present a schematic illustration and magnified optical image of a representative μ -ILED, respectively. These design choices are informed by careful studies of the mechanics through three-dimensional finite-element modelling (3D-FEM) of the complete systems; they represent highly optimized versions of those reported recently for silicon circuits²⁰ and μ -ILEDs (ref. 18). The results enable stable and robust operation during large-scale uniaxial,

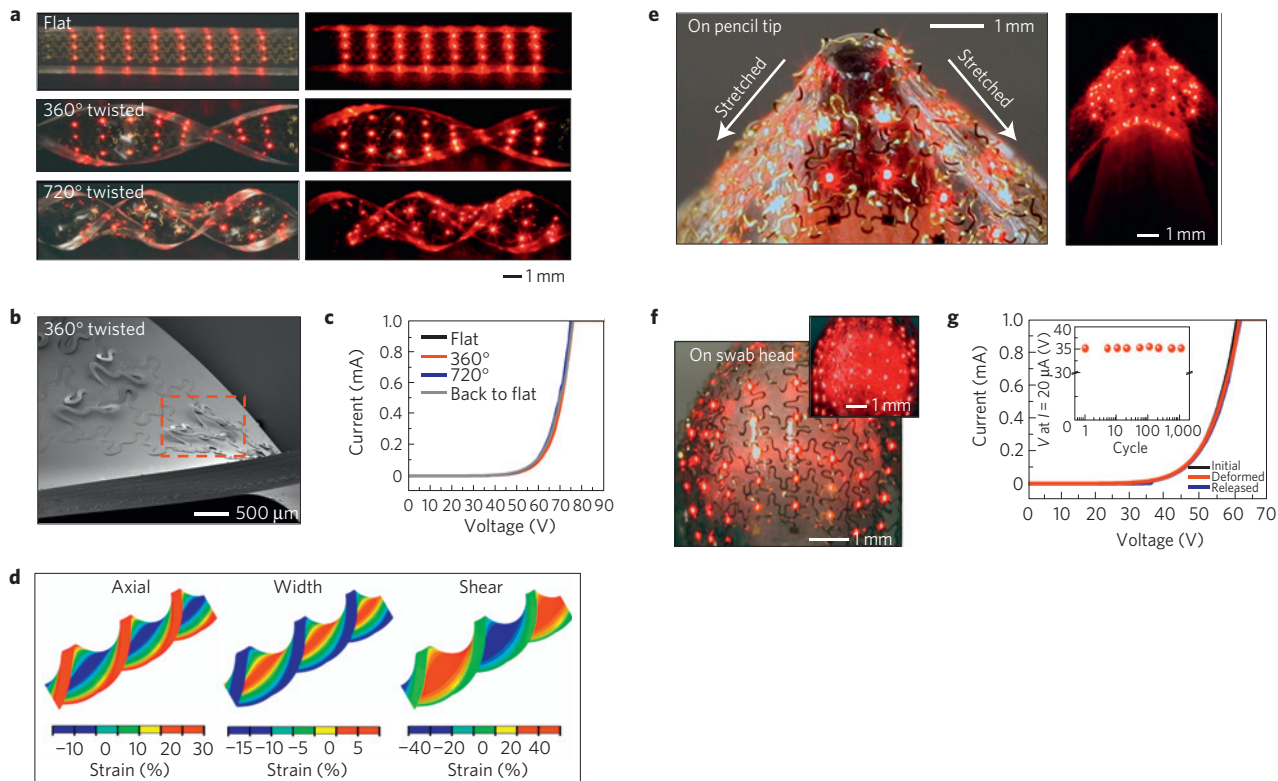


Figure 2 | Responses of μ -ILED arrays to twisting and to stretching on sharp tips. **a**, Optical images of an array of μ -ILEDs (3×8) on a band of PDMS twisted to different angles (0° (flat), 360° and 720° from top to bottom), collected with (left) and without (right) external illumination. **b**, Scanning electron microscope image of the array when twisted to 360° . The serpentine interconnects move out of the plane (red box) to accommodate the induced strains. **c**, I - V characteristics of the array twisted by various amounts (0 (flat), 360 and 720°). **d**, Distributions of axial, width and shear strain determined by 3D-FEM for twisting to 720° . **e**, Optical images of an array of μ -ILEDs (6×6), tightly stretched on the sharp tip of a pencil, collected with (left) and without (right) external illumination. The white arrows indicate the direction of stretching. **f**, Optical images of a stretchable 8×8 array wrapped and stretched downward on the head of a cotton swab. The inset image was obtained without external illumination. **g**, I - V characteristics of the array in **e**, before (initial), during (deformed) and after (released) deformation. The inset provides a graph of the voltage needed to generate a current of $20 \mu\text{A}$, measured after different numbers of cycles of deformation.

biaxial, shear and other mixed modes of deformation, as described in the following.

Supplementary Figs S4a and S5a show tilted-view scanning electron microscope images and corresponding optical microscope images of adjacent μ -ILEDs and non-coplanar serpentine interconnects formed with $\sim 20\%$ biaxial prestrain before (left) and after (right) uniaxial stretching ($\sim 60\%$), respectively. The separations between adjacent pixels change by an amount expected from the prestrain and the applied strain, where a combination of in- and out-of-plane conformational changes in the serpentines accommodates the resulting deformations in a way that avoids any significant strains at the positions of the μ -ILEDs. In particular, 3D-FEM modelling results (Supplementary Fig. S4b) reveal peak strains in the metal interconnect and the μ -ILEDs that are more than 300 times smaller than the applied strain. (Supplementary Fig. S5c shows similar results for $\sim 59\%$ stretching along the diagonal direction, corresponding to Supplementary Fig. S5b.) Figure 1b and Supplementary Fig. S6 present two-dimensional, in-plane stretching of a 6×6 array of μ -ILEDs along horizontal (left) and diagonal (right) directions. The uniform and constant operating characteristics of all devices are clearly apparent in the dark and bright (without and with external illumination) images of Fig. 1b and Supplementary Fig. S6 as well as in the current–voltage (I – V) characteristics (left-hand frame of Fig. 1c). The applied strains, calculated from the separations of inner edges of adjacent pixels before and after stretching, reach $\sim 48\%$ and $\sim 46\%$ along the horizontal and diagonal directions, respectively. The I – V characteristics

are invariant even after 100,000 cycles of 75% stretching along the horizontal direction (right-hand frame of Fig. 1c).

Uniaxial stretching and compression are among the simplest modes of deformation. Others of interest include biaxial, shear and related. The results of Fig. 1d–g and Supplementary Fig. S7 demonstrate the ability of the reported designs to enable this first type of motion, through large strains induced by pneumatic pressure, achieved by inflation of a thin ($500 \mu\text{m}$) membrane of PDMS that supports an array similar to that of Fig. 1b. Injecting air through a syringe into a specially designed cylinder that serves as a mount for the device deforms the initially flat array (top frame of Fig. 1d) into a balloon shape (bottom frame of Fig. 1d). Figure 1e shows four pixels in the ‘flat’ (top) and ‘inflated’ states (bottom) during operation, with external illumination. The area expansion induced in this manner can reach $\sim 85\%$ without any device failures. The I – V characteristics also show no appreciable differences between the flat and inflated states (Fig. 1f). 3D-FEM is used to model the inflation-induced deformation of a circular elastomeric membrane, with the same thickness ($500 \mu\text{m}$) and diameter (20 mm) as in experiment, but without a mounted μ -ILED array. As illustrated in Fig. 1g and Supplementary Fig. S7c, both the circumferential and meridional strains reach $\sim 37.3\%$ when inflated to a height of 8.3 mm , the same as in the bottom frame of Fig. 1d. Measured displacements of devices in the system of the bottom frame of Fig. 1e indicate strains of $\sim 36\%$, which are comparable to values calculated by 3D-FEM. This observation suggests an important conclusion: with the designs reported here, the arrays

provide negligible mechanical loading of the soft, elastomeric membrane support, consistent with the very low effective modulus provided by the optimized, non-coplanar serpentine.

Corkscrew twisting (Fig. 2a) provides another well-defined mode of deformation that is of interest. Here, large shear strains occur in addition to stretching–compression in the axial and width directions. The device test structure in this case consists of a 3×8 array of μ -ILEDs transferred to a band of PDMS without prestrain (see Supplementary Fig. S8a for details). Optical images of flat, 360° and 720° twisting deformations with (left) and without (right) external illumination (Fig. 2a) reveal uniform and invariant emission. These strains lead to out-of-plane motions of the serpentine, as shown in Fig. 2b and Supplementary Fig. S8b. The μ -ILEDs remain attached to the PDMS substrate owing to their strong bonding²⁰. Electrical measurements indicate similar I – V characteristics with different twisting angles (Fig. 2c) and at different stages of fatigue tests, as shown in Supplementary Fig. S8c. Figure 2d presents distributions of various strain components, evaluated at the surface of a band of PDMS with thickness 0.7 mm by 3D-FEM: axial stretching (left-hand frame), width stretching (middle frame) and shear (right-hand frame) (for 360° twisting, see Supplementary Fig. S9). The results demonstrate that the PDMS surface undergoes both extreme axial/width stretching and shear deformations, with shear dominating, and reaching values of $\sim 40\%$ for the 720° twist. As for the case of Fig. 1d,g, the distributions of strain for the bare PDMS substrate can provide reasonably good estimates for the system. These controlled uniaxial (Fig. 1b), biaxial (Fig. 1d) and twisting (Fig. 2a) modes suggest an ability to accommodate arbitrary deformations. As two examples, Fig. 2e,f shows cases of stretching onto the sharp tip of a pencil and wrapped onto a cotton swab. The array of 6×6 μ -ILEDs pulled onto the pencil (red arrows indicate stretching directions) experiences local, peak strains of up to $\sim 100\%$, estimated from distances between adjacent devices in this region. Similar but milder and more spatially distributed deformations occur on the cotton swab, with an 8×8 array. In both cases, observation and measurement indicate invariant characteristics, without failures, even during fatigue tests (Fig. 2g and Supplementary Fig. S10).

A key feature of the layouts that enable these responses is the relatively small area coverage of active devices, such that the serpentine structures can absorb most of the motions associated with applied strain. An associated disadvantage, for certain applications, is that only a small part of the overall system emits light. This limitation can be circumvented with layouts that consist of multilayer stacks of devices, in laminated configurations, with suitable spatial offsets between layers. The exploded-view schematic illustration in Fig. 3a shows this concept with four layers. Supplementary Fig. S11 provides details. Integration is accomplished with thin coatings of PDMS ($\sim 300\text{ }\mu\text{m}$) that serve simultaneously as elastomeric interlayer dielectrics, encapsulants and adhesives. Here, each layer consists of a substrate of PDMS ($300\text{ }\mu\text{m}$ thick) and an array of LEDs (total thickness with interconnect $\sim 8\text{ }\mu\text{m}$). The total thickness of the four-layer system, including interlayers of PDMS, is $\sim 1.3\text{ mm}$. Optical images of emission from a four-layer system appear in Fig. 3b (with external illumination) and Supplementary Fig. S11b (without external illumination). Figure 3c shows a two-layer case, where each layer illuminates in a different pattern. The inset on the right illustrates the same system in a bent state (bending radius = 2 mm), where the maximum strain in top and bottom GaAs layers is only 0.006% and 0.007%, respectively, as shown by 3D-FEM simulation (Supplementary Fig. S12). The PDMS interlayers restrict the motion of the serpentine, but by an amount that reduces only slightly the overall deformability. The extent of free movement can be maximized by minimizing the modulus of the encapsulant. We used PDMS mixed in a ratio to yield a value for Young's modulus of $\sim 0.1\text{ MPa}$ (ref. 21), to retain nearly $\sim 90\%$ of the stretchability of the unencapsulated case²².

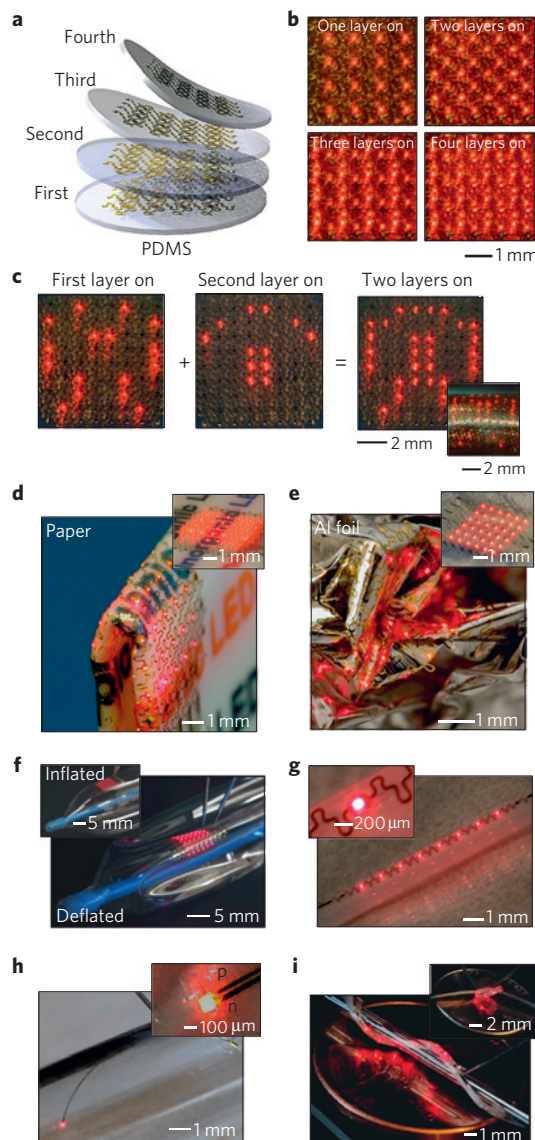


Figure 3 | Multilayer laminated configurations of arrays of μ -ILEDs for high effective area coverage and integration on various unusual substrates. **a**, Schematic, exploded-view illustration of a stacked device formed by multilayer lamination. **b**, Optical images of a four-layer stack of 4×4 arrays with layer-to-layer offsets designed to minimize overlap of interconnect lines with positions of the μ -ILEDs. The images show emission with different numbers of layers in operation (first layer on, first and second layers on, first, second and third layers on and first, second, third and fourth layers on). **c**, Optical images of a two-layer stack of 8×8 arrays, with different layers in operation. The inset shows the device in a bent state (bending radius $\sim 2\text{ mm}$) with both layers on. **d**, Optical image of an array of μ -ILEDs (8×8) on a piece of paper, in a folded state (bending radius $\sim 400\text{ }\mu\text{m}$) during operation. The inset shows the device in its flat state. **e**, Image of a 6×6 array on a sheet of aluminium foil in a crumpled state. The inset shows the device in its flat state. **f**, Images of a 6×6 array on a catheter balloon in its inflated (inset) and deflated states. **g**, Images of a thin ($\sim 8\text{ }\mu\text{m}$), narrow ($820\text{ }\mu\text{m}$) strip of μ -ILEDs (1×8) with serpentine interconnects on a rigid plastic tube (diameter $\sim 2.0\text{ mm}$, left). Inset: magnified view of a single pixel. **h**, A thin-strip LED device consisting of an isolated μ -ILED with straight interconnects wrapped around a glass tube (diameter $\sim 5.0\text{ mm}$, right). The inset provides a magnified view. **i**, Image of a 1×8 array with serpentine metal bridges on a $\sim 700\text{-}\mu\text{m}$ -diameter fibre, wrapped around a glass tube (diameter $\sim 1.4\text{ mm}$) and in a knotted state (inset), resting on coins (pennies) to set the scale.

The favourable mechanical characteristics enable integration onto a variety of substrates that are incompatible with conventional optoelectronics. As demonstrations, we built μ -ILED devices on swatches of fabric (Supplementary Fig. S13a), tree leaves (Supplementary Fig. S13c), sheets of paper (Fig. 3d), pieces of aluminium foil (Fig. 3e) and balloon catheters (Fig. 3f). In all cases, transfer printing successfully delivers the devices to these substrates with thin ($\sim 50 \mu\text{m}$) coatings of PDMS that serve as planarizing and strain-isolating layers, and as adhesives²³. Bending and folding tests for each case indicate robust operation under deformed states. The smallest bending radii explored experimentally were 4 mm, 2.5 mm and $400 \mu\text{m}$ for the fabric, leaf and paper, respectively. Theoretical modelling²³, using Young's moduli and thicknesses 1.2 MPa, 800 μm , 23.5 MPa, 500 μm , 600 MPa and 200 μm for the fabric, leaf and paper^{24–26}, respectively, shows that the fabric, leaf and paper can be completely folded, in the sense that the strain in the GaAs remains much smaller than its failure strain ($\sim 1\%$) even when the bend radius equals the substrate thickness (see Supplementary Information for details). Without the strain isolation provided by the PDMS, the fabric can still be folded, but the leaf and paper can only be bent to minimal radii of 1.3 mm and 3.5 mm, respectively. This result occurs because Young's modulus of PDMS (0.4 MPa) is much smaller than those of leaf and paper (that is, strain isolation), whereas Young's moduli of PDMS and fabric are more similar. Random wrinkling, including multidirectional folding with inward and outward bending, can be accommodated, as is apparent in the devices on paper and aluminium foil ($\sim 30 \mu\text{m}$). In images of the latter case (Fig. 3e), the number density of wrinkles reaches $\sim 200 \text{ cm}^{-2}$ with approximate radii of curvature as small as $150 \mu\text{m}$ (see Supplementary Figs S13–15 for extra images, plots of I – V characteristics, results of fatigue tests and surface topography of these substrates).

The arrays of μ -ILEDs mounted on the surface of an otherwise conventional catheter balloon (Fig. 3f) could enable highly localized photodynamic drug delivery to treat selectively a variety of intraluminal tumours and cardiovascular disorders, including atherosclerotic plaque lesions^{27–30}. Phototherapy (for example, stabilization of plaque) and spectroscopic characterization of arterial tissue^{31–33} represent other possibilities. Thin threads and fibres represent other substrates of potential biomedical interest, owing to their potential for use as sutures and implants, as described next. Figure 3g,h presents images of an array of μ -ILEDs (1×8) with serpentine metal bridges and a single μ -ILED device with long ($1.25 \text{ cm} \times 185 \mu\text{m}$) metal interconnects, both on flexible, thin ($\sim 8 \mu\text{m}$) ribbons mounted onto cylindrical supports. Figure 3i shows related systems, consisting of μ -ILED arrays on pieces of thread, and wrapped around a rod and tied in a knot (inset). We explored threads of nylon (Fig. 3i) and cotton (Supplementary Fig. S16a–c), with diameters of $\sim 0.7 \text{ mm}$, $\sim 2.5 \text{ mm}$, and $\sim 0.7 \text{ mm}$, $\sim 0.3 \text{ mm}$, respectively. Integration on these and other small substrates is challenging with the usual techniques for transfer printing. Instead, we rolled these threads over the glass carrier substrate in a manner that avoided the use of a separate transfer stamp and the associated difficulties in alignment and contact (see Supplementary Fig. S16d–e). As clearly illustrated in Fig. 3i, the optimized mechanical designs described previously enable these systems to be twisted, bent and tied into knots without affecting the operation, even when encapsulated with PDMS. The approximate minimum bending radius for the main frame and inset of Fig. 3i is $\sim 3 \text{ mm}$ and $\sim 0.7 \text{ mm}$, respectively.

Figure 4a demonstrates the use of a device like those in Fig. 3i as a light-emitting suture in an animal model, manipulated with a conventional suture needle starting from the initial incision (upper left) to the completion of three stitches (lower left; Supplementary Fig. S16f shows an incised paper sheet sutured with a similar device, in a similar manner). The 1×4 array of μ -ILEDs in this

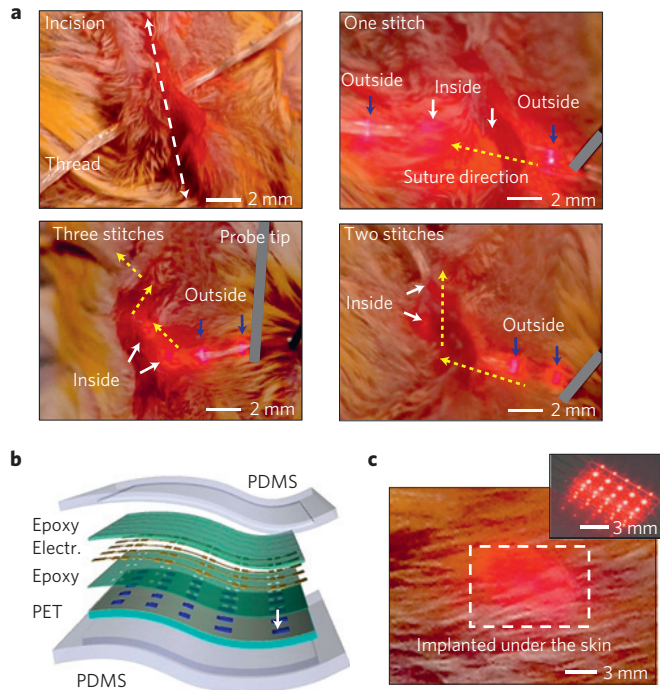


Figure 4 | Demonstrations of application possibilities for systems of μ -ILEDs in biomedicine. **a**, Light-emitting suture consisting of a 1×4 array of μ -ILEDs on a thread (diameter $\sim 700 \mu\text{m}$), demonstrated in an animal model with a conventional suture needle. The images correspond to one stitch in its off state, after one stitch, two stitches and three stitches in the on state, in the clockwise direction from the top left-hand frame, respectively. The yellow arrows indicate the suturing directions. **b**, Schematic exploded-view illustration of an array of μ -ILEDs (5×5) on a thin PET film ($50 \mu\text{m}$ thick) coated with an adhesive. Layers of PDMS on the top and bottom provide a soft, elastomeric encapsulation that offers biocompatibility and an excellent barrier to biofluids and surrounding tissue. **c**, Image of an animal model with this array implanted under the skin, and on top of the muscle tissue. The inset shows the device before implantation.

case operates without any failures, owing partly to favourable mechanics as described previously but also to a fully encapsulating layer of PDMS as a soft, elastomeric and biocompatible barrier to the surrounding tissue and associated biofluids. This layer prevents device degradation and electrical shorting through the surrounding biofluid or to the tissue; its low modulus avoids any significant alteration in the overall mechanics, as described previously. The frames in Fig. 4a show a few of the μ -ILEDs in the array deployed subcutaneously, and others on the outer epidermis layer of skin. (The white and blue arrows in the images correspond to pixels located on the subdermal and epidermal layers, respectively. The yellow dotted arrows highlight the stitch directions.) We predict use of such ‘photonic’, or ‘light-emitting’, sutures for accelerated healing^{34–38} and for transducers of vital signs or physiological parameters such as blood oxygenation and perfusion. Alternatively, for longer-term implantable applications, subdermal μ -ILEDs can overcome scattering limitations and bring *in vivo* illumination to deep layers of tissue. This approach could yield capabilities complementary to those of fibre-optic probe-based medical spectroscopic methods, by enabling real-time evaluation of deep-tissue pathology while enabling precise delivery of radiation in programmable arrays. Such devices can be formed in geometries of strips or threads, or of sheets. As an example of the latter, the left-hand frames of Fig. 4b and Supplementary Fig. S17 show a schematic exploded view and an illustration of

fabrication procedures, respectively, for a 5×5 array of μ -ILEDs on a thin sheet of polyethylene terephthalate (PET; Grafix DURA-RAR, 50- μm -thickness) film coated with an adhesive layer (epoxy) and encapsulated on the top and bottom with PDMS. Thin ($\sim 500 \mu\text{m}$) ceramic insulated gold wires that connect to metal pads at the periphery of the array provide access to external power supplies. Figure 4c presents a picture of an animal model with the device implanted subdermally in direct contact with the underlying musculature (see Methods for details). The inset shows the same device before implantation. For continuous operation at the current levels reported here, we estimate peak increases in temperature at the tissue of a couple of degrees Celsius. Short-pulsed-mode operation could further minimize the possibility of adverse thermal effects and also, at the same time, enable the use of phase-sensitive detection techniques for increasingly sophisticated diagnostics, imaging and physiological monitoring.

Use of μ -ILED technologies in such applications requires integrated photonic structures for transmission-collection of light and/or for optical sensing of surface binding events or changes in local index of refraction. In this context, plasmonic crystals represent a useful class of component, particularly for the latter purposes. Figure 5 summarizes an illuminated sensor device that combines thin, moulded plasmonic crystals with arrays of μ -ILEDs, in a tape-like format that can be integrated directly on flexible tubing suitable for use in intravenous delivery systems, for monitoring purposes. Figure 5a provides an exploded-view schematic illustration of the system. The plasmonic structure, similar to those described recently³⁹, consists of a uniform layer of Au (50 nm) sputter deposited onto a thin polymer film embossed with a square array of cylindrical holes (that is, depressions) using the techniques of soft lithography, as illustrated in Fig. 5b,c. The relief geometry (depth $\sim 200 \text{ nm}$; hole diameter $\sim 260 \text{ nm}$; pitch $\sim 520 \text{ nm}$; see Fig. 5c, and inset of Fig. 5d) and thickness of the Au were optimized to yield measurable changes in transmission associated with surface binding events or variations in the surrounding index of refraction at the emission wavelength of the μ -ILEDs (ref. 40). The full spectral responses appear in Supplementary Fig. S18. Figure 5d provides transmittance data measured using a spectrometer over a relevant range of wavelengths, for different surrounding fluids. (See Methods for details.) The completed microsensor devices appear in Fig. 5e,f. As different fluids flow through the tubing, the amount of light that passes from the μ -ILEDs and through the integrated plasmonic crystal changes, to provide highly sensitive, quantitative measurements of the index of refraction. The data of Fig. 5g show the response of a representative tube-integrated device, and comparison with calculations based on data from corresponding plasmonic structures on rigid substrates, immersed in bulk fluids and probed with a conventional, bench-scale spectrometer (Supplementary Figs S18,S19). This kind of system can be used for continuous monitoring of the dosage of nutrients, such as glucose illustrated here, or of polyethylene glycol as illustrated in Supplementary Information, or other biomaterials of relevance for clinical medicine.

Integration of μ -IPDs with such sensors can yield complete, functional systems. To demonstrate this type of capability and also another application example, we built a flexible, short-range proximity sensor that could be mounted on machine parts, or robotic manipulators, or for use in instrumented surgical gloves. This device exploits co-integration of μ -ILEDs and μ -IPDs in a stretchable format that provides both a source of light and an ability to measure backscatter from a proximal object. The intensity of this backscatter can be correlated to the distance from the object. The μ -IPDs use reverse-biased GaAs diodes as functional, although inefficient, detectors of light emitted from the μ -ILEDs. A schematic diagram of the integrated system appears in Fig. 6a.

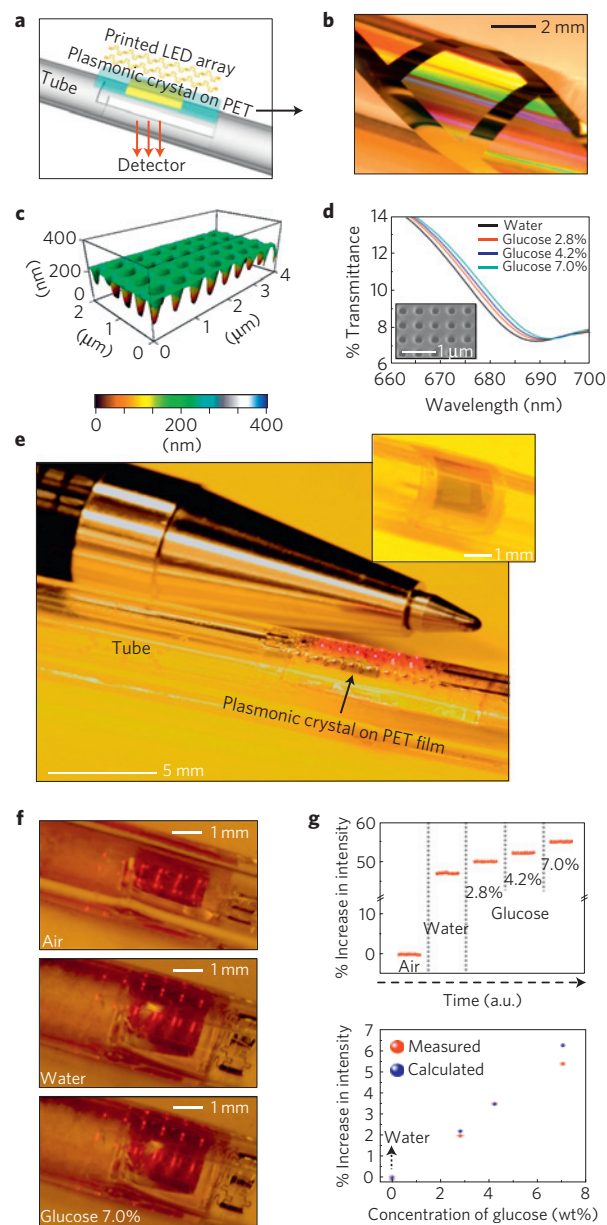


Figure 5 | Refractive-index microsensors based on thin, moulded plasmonic crystals integrated with arrays of μ -LEDs, in tape-like formats integrated directly on flexible tubing suitable for use in intravenous delivery systems. **a**, Schematic exploded view of the sensor-tube system. **b**, Thin, moulded plasmonic crystal on a plastic substrate wrapped around a cylindrical support, showing colours due to diffraction. **c**, Atomic force microscope image of the surface of such a crystal. **d**, Normal-incidence transmission spectra collected with a commercial spectrometer over a range of wavelengths relevant for illumination with red μ -LEDs. **e**, Image of a sensor integrated on an flexible plastic tube (Tygon), next to the tip of a pen. The inset shows the backside of the plasmonic crystal before integration of the μ -LEDs. **f**, Images of the tube-integrated sensor viewed from the μ -ILED side of the device, with different fluids in the tube. **g**, Measurement results from a representative sensor (top), operated while integrated with a tube, as a sequence of aqueous solutions of glucose passes through. The bottom frame shows the percentage increase in light transmitted from the μ -ILED, through the plasmonic crystal, and measured on the opposite side of the tube with a silicon photodiode, as a function of glucose concentration. The calculations are based on the response of a separate, conventional plasmonic crystal evaluated using bulk solutions and a commercial spectrometer.

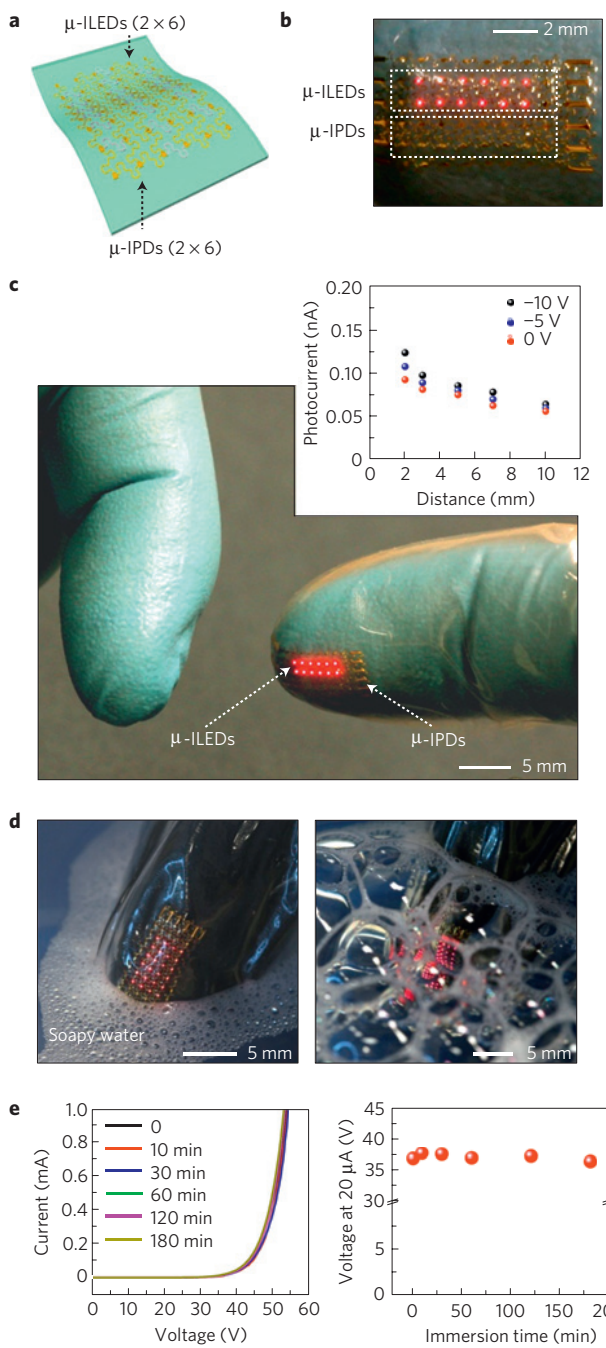


Figure 6 | Stretchable optical proximity sensor consisting of an array of μ -LEDs and μ -IPDs mounted on the fingertip of a vinyl glove.

a, Schematic illustration of cointegrated 2×6 arrays of μ -LEDs and μ -IPDs to yield a thin, stretchable optical proximity sensor. **b**, Image of the sensor, mounted on the fingertip region of a vinyl glove. **c**, Optical images of an array of μ -LEDs (4×6) with serpentine metal bridges, transfer printed on the fingertip region of a vinyl glove. The inset shows a plot of photocurrent as a function of distance between the sensor and an object (white filter paper) for different reverse biases and different voltages. **d**, Left- and right-hand frames correspond to images before and after immersion into soapy water. **e**, Intravenous characteristics of the same μ -LED array as shown in **c** after operation in saline solution (~9%) for different immersion times.

Figure 6b,c shows this type of system, with 4×6 arrays of μ -LEDs and μ -IPDs, integrated onto the fingertip region of a vinyl glove. As expected, the photocurrent measured at the μ -IPDs increases

monotonically with decreasing distance from the object, as shown in the inset of Fig. 6c for different reverse bias voltages (-10 , -5 and 0 V). (Supplementary Fig. S20a provides I - V characteristics of μ -IPDs.) Stacked geometries, such as those presented in Fig. 3d, can also be used, as shown in Supplementary Figs. S20b–e. Similar to other devices described here, encapsulation with PDMS renders the systems waterproof. The left- and right-hand frames of Fig. 6d show images of a 4×6 array of μ -LEDs on a vinyl glove, before and after immersion in soapy water. The uniform light-emission characteristics of all devices in the array are clearly apparent. I - V characteristics are invariant even after operation in saline solution (~9%) for 3 h (Fig. 6e) and 1,000 cycles of immersion (Supplementary Fig. S21) in this solution (Fig. 6e), proving the robust operation of this device inside the body or during use in a surgical procedure.

In summary, the advances reported here in mechanics, high-fill-factor multilayer layouts and biocompatible designs provide important, unusual capabilities in inorganic optoelectronics, as demonstrated by successful integration onto various classes of substrate and by use in representative devices for biomedical and robotics applications. Areas for further work range from the development of related strategies for μ -LEDs based on materials such as GaN to multispectral biomedical systems suitable for clinical use.

Methods

Delineating semiconductor material for μ -LEDs and μ -IPDs. Fabrication of the μ -LEDs followed procedures reported elsewhere. The μ -IPDs relied on similar strategies. Briefly, the process began with epitaxial films that included a quantum-well structure ($4 \times$ (6-nm-thick $\text{Al}_{0.25}\text{Ga}_{0.25}\text{In}_{0.5}\text{P}$ barriers/6-nm-thick $\text{In}_{0.56}\text{Ga}_{0.44}\text{P}$ wells)/6-nm-thick $\text{Al}_{0.25}\text{Ga}_{0.25}\text{In}_{0.5}\text{P}$ barriers) and an underlying sacrificial layer of $\text{Al}_{0.96}\text{Ga}_{0.04}\text{As}$ on a GaAs wafer. Details appear in Supplementary Fig. S1a. Inductively coupled plasma reactive ion etching (Unaxis SLR 770 system) with $\text{Cl}_2\text{-H}_2$ through a hard mask of SiO_2 formed trenches down to the $\text{Al}_{0.96}\text{Ga}_{0.04}\text{As}$, to delineate active materials in 6×6 , 8×8 , 3×8 or 1×4 arrays of squares with sizes of $100 \mu\text{m} \times 100 \mu\text{m}$. Next, photolithography defined photoresist structures at the four corners of each square to hold the epitaxial layers to the underlying GaAs wafer during removal of the $\text{Al}_{0.96}\text{Ga}_{0.04}\text{As}$ with diluted HF (Transene, USA) (deionized water (DI):49% HF = 1:100).

Fabricating arrays of μ -LEDs and μ -IPDs. The released squares of epitaxial material formed according to procedures described above were transfer printed onto a glass substrate coated with layers of a photodefinition epoxy (SU8-2; Microchem.; 1.2 μm thick), polyimide (Sigma-Aldrich; 1.2 μm thick) and PMMA A2 (Microchem.; 100 nm thick) from top to bottom. Next, another layer of epoxy (SU8-2, 2.0 μm) was spin-cast and then removed everywhere except from the sidewalls of the squares by reactive ion etching (PlasmaTherm 790 series) to reduce the possibility of partial removal of the bottom n-GaAs layer during the first step of an etching process (first step, $\text{H}_3\text{PO}_4:\text{H}_2\text{O}_2:\text{DI} = 1:13:12$ for 25 s; second step, $\text{HCl}:\text{DI} = 2:1$ for 15 s; third step, $\text{H}_3\text{PO}_4:\text{H}_2\text{O}_2:\text{DI} = 1:13:12$ for 24 s) that exposed the bottom n-GaAs layer for ncontacts. Next, another layer of epoxy (1.2 μm thick) spin-cast and photopatterned to expose only certain regions of the top p-GaAs and bottom n-GaAs provided access for metal contacts (non-Ohmic contacts) and interconnect lines (Cr–Au, 30 nm–300 nm) deposited by electron-beam evaporation and patterned by photolithography and etching. These lines connected devices in given row in series, and adjacent rows in parallel. A final layer of spin-cast epoxy (2.5 μm) placed the devices and metal interconnects near the neutral mechanical plane. Next, the underlying polymer layers (epoxy–polyimide–PMMA) were removed from regions not protected by a masking layer of SiO_2 (150 nm thick) by reactive ion etching (oxygen plasma, 20 s.c.c.m., 150 mtorr, 150 W, 40 min). Wet etching the remaining SiO_2 with buffered oxide etchant exposed the metal pads for electrical probing, thereby completing the processing of arrays of μ -LEDs (and/or μ -IPDs) with serpentine interconnects.

Transfer printing devices to substrates of interest. Dissolving the PMMA layer of the structure described above with acetone at 75 °C for 10 min released the interconnected array of devices from the glass substrate. Lifting the array onto a flat elastomeric stamp and then evaporating layers of Cr/SiO₂ (3 nm/30 nm) selectively onto the backsides of the devices enabled strong adhesion to sheets or strips of PDMS or to other substrates coated with PDMS. For the PDMS balloon of Fig. 1d, we applied prestrain by partially inflating the balloon, transfer printed the μ -LEDs and then released (deflated) the balloon. For small substrates, roller-printing techniques were used. See Supplementary Information for details.

Stretching tests and electrical characterization. Stretching tests were made using custom assemblies of manually controlled mechanical stages, capable of applying strains along x , y and diagonal directions. For fatigue testing, one cycle corresponds to deformation to a certain level and then return to the undeformed state. Each fatigue test was carried out up to 1,000 cycles to levels of strains similar to those shown in the various figures. Electrical measurements were conducted using a probe station (4155C; Agilent), by directly contacting metal pads while stretched, bent or twisted. For Fig. 2d, the measurement was carried out using a lead-out conductor line, bonded to metal pads of the arrays of μ -ILEDs. Typical voltage-scan ranges for measurement of the 6×6 , 8×8 and 3×8 arrays were 0–60 V, 0–80 V and 0–90 V, respectively.

Animal experiments. All procedures were carried out under approved animal protocols. A female Balb/c mouse was anaesthetized with an intraperitoneal injection of a mix of ketamine–xylazine. The depth of anaesthesia was monitored by palpebral and withdrawal reflexes to confirm that the animal had reached ‘stage 3’ of anaesthesia. Once the animal was lightly anaesthetized, the back was shaved and cleaned at the incision site with 70% ethanol, followed by a betadine surgical scrub. Previous implants were removed from the mouse and the animal was euthanized according to approved protocols. To validate the performance of sutures in real conditions, the incision opened during surgery was closed with a customized 16-gauge needle and three passes with the light-emitting suture were carried out to seal the wound. The suture was then tested by verifying the proper operation of the μ -ILEDs. For the implants, the incision was carried out on the dorsal side of the mouse and the suturing was carried out across the dermal layers (outer layers and subcutaneous tissues) above the muscle tissue.

Fabrication of thin plasmonic crystals on plastic. We used techniques of soft lithography and previously reported procedures to form structures of surface relief on thin layers of a photocurable polyurethane (PU, NOA 73, Norland Products) cast onto sheets of PET. Sputter deposition (5 mtorr Ar environment; AJA sputtering system) of uniform, thin (~ 50 nm) layers of gold completed the fabrication. The geometry of the relief and the thickness of the gold were selected to optimize the performance of the plasmonic crystals at the emission wavelength of the μ -ILEDs.

Spectroscopic measurement of the plasmonic crystals. Transmission spectra were measured using a Varian 5G UV–Vis–NIR spectrophotometer operating in normal-incidence transmission mode, without temperature control. A flow cell was mounted on top of the plasmonic crystal and aqueous solutions of glucose with different concentrations–refractive indexes were injected with a syringe pump (Harvard Apparatus) at a flow rate of 0.2 ml min^{-1} . Transmission spectra over a wavelength range of 355–1,400 nm were collected during the process to monitor changes in multiple plasmonic responses. Such data were used in the process of optimizing the layouts of the crystals, and for interpreting measurements collected with the flexible, illuminated and tube-integrated sensors.

Fabrication and testing of illuminated plasmonic crystal sensors. The procedure for integrating a plasmonic crystal with μ -ILED light sources on a tube (Tygon R-3603, inner and outer diameter: 0.318 mm and 0.476 mm, respectively) began with formation of a contact window by cutting an opening in the tube, to enable direct contact of fluid in the tube with the plasmonic crystal. The embossed side of the crystal was placed face down against the window and then sealed with a transparent adhesive tape. Next, a thin layer of PDMS was coated on the tape and adjacent regions of the tubing as a bonding layer for a transfer-printed, stretchable array of μ -ILEDs aligned to the plasmonic crystal. This step completes the integration process. Light from the device was collected with a separate, commercial Si photodetector (ThorLabs, Model DET110) placed on the opposite side of the tubing. Output from the detector was sampled digitally at a rate of 10 kHz. Averaging times of 6 s were used for each recorded data point.

Photographs. Images in Figs 1a and 3e were combined images to eliminate out-of-focus regions. Tens of pictures were captured at different focal depths using a Canon 1Ds Mark III with a Canon MP-E 1.5x Macro lens, and these captured pictures were merged in the software ‘Helicon Focus’ to create a completely focused image from several partially focused images.

Received 5 April 2010; accepted 13 September 2010;
published online 17 October 2010

References

- Reuss, R. H. *et al.* Macroelectronics: Perspectives on technology and applications. *Proc. IEEE* **93**, 1239–1256 (2005).
- Forrest, S. R. The path to ubiquitous and low cost organic electronic appliances on plastic. *Nature* **428**, 911–918 (2004).
- Menard, E. *et al.* Micro- and nanopatterning techniques for organic electronic and optoelectronic systems. *Chem. Rev.* **107**, 1117–1160 (2007).
- Loo, Y-L. & McCulloch, I. Progress and challenges in commercialization of organic electronics. *MRS Bull.* **33**, 653–662 (2008).
- So, F., Kido, J. & Burrows, P. Organic light-emitting devices for solid-state lighting. *MRS Bull.* **33**, 663–669 (2008).
- Razavi, F. H. *et al.* Three dimensional nanopillar array photovoltaics on low cost and flexible substrates. *Nature Mater.* **8**, 648–653 (2009).
- Ko, H. *et al.* Flexible carbon nanofiber connectors with anisotropic adhesion properties. *Small* **6**, 22–26 (2010).
- Cohen-Karni, T., Timko, B. P., Weiss, L. E. & Lieber, C. M. Flexible electrical recording from cells using nanowire transistor arrays. *Proc. Natl Acad. Sci. USA* **106**, 7309–7313 (2009).
- Timko, B. P. *et al.* Electrical recording from hearts with flexible nanowire device arrays. *Nano Lett.* **9**, 914–918 (2009).
- Siegel, A. C., Philips, S. T., Wiley, B. J. & Whitesides, G. M. Thin, lightweight, foldable thermochromic displays on paper. *Lab Chip* **9**, 2775–2781 (2009).
- Siegel, A. C. *et al.* Foldable printed circuit boards on paper substrates. *Adv. Funct. Mater.* **20**, 28–35 (2010).
- Hu, L. *et al.* Highly conductive paper for energy-storage devices. *Proc. Natl Acad. Sci. USA* **106**, 21490–21494 (2009).
- Hu, L. *et al.* Stretchable, porous, and conductive energy textiles. *Nano Lett.* **10**, 708–714 (2010).
- Sekitani, T. *et al.* Stretchable active-matrix organic light-emitting diode display using printable elastic conductors. *Nature Mater.* **8**, 494–499 (2009).
- Jacobs, H. O. & Whitesides, G. M. Submicrometer patterning of charge in thin-film electrets. *Science* **291**, 1763–1766 (2001).
- Cole, J., Wang, X. & Jacobs, H. O. Patterned growth and transfer of ZnO micro- and nanocrystals with size and location control. *Adv. Mater.* **20**, 1474–1478 (2008).
- Leong, T. G. *et al.* Tetherless thermobiochemical actuated microgrippers. *Proc. Natl Acad. Sci. USA* **106**, 703–709 (2009).
- Park, S-I. *et al.* Printed assemblies of inorganic light-emitting diodes for deformable and semitransparent displays. *Science* **325**, 977–981 (2009).
- Dupuis, D. R. & Krames, M. R. History, development, and applications of high-brightness visible light-emitting diodes. *IEEE J. Lightwave Technol.* **26**, 1154–1171 (2008).
- Kim, D-H. *et al.* Materials and noncoplanar mesh designs for integrated circuits with linear elastic responses to extreme mechanical deformations. *Proc. Natl Acad. Sci. USA* **105**, 18675–18680 (2008).
- Brown, X. Q., Ookawa, K. & Wong, J. Y. Evaluation of polydimethylsiloxane scaffolds with physiologically-relevant elastic moduli: Interplay of substrate mechanics and surface chemistry effects on vascular smooth muscle cell response. *Biomaterials* **26**, 3123–3129 (2005).
- Kim, D-H. *et al.* Optimized structural designs for stretchable silicon integrated circuits. *Small* **5**, 2841–2847 (2009).
- Kim, D-H. *et al.* Ultrathin silicon circuits with strain-isolation layers and mesh layouts for high-performance electronics on fabric, vinyl, leather, and paper. *Adv. Mater.* **21**, 3703–3707 (2009).
- Jeon, B. S., Chun, S. Y. & Hong, C. J. Structural and mechanical properties of woven fabrics employing Peirce’s model. *Tex. Res. J.* **73**, 929–933 (2003).
- Gardner, W. R. & Ehlig, C. F. Physical aspects of the internal water relations of plant leaves. *Plant Physiol.* **40**, 705–710 (1965).
- Cox, H. L. The elasticity and strength of paper and other fibrous materials. *Br. J. Appl. Phys.* **3**, 72–79 (1952).
- Hayase, M. *et al.* Photoangioplasty with local motexafin lutetium delivery reduces macrophages in a rabbit post-balloon injury model. *Cardiovasc. Res.* **49**, 449–455 (2001).
- Waksman, R. *et al.* Photopoint photodynamic therapy promotes stabilization of atherosclerotic plaques and inhibits plaque progression. *J. Am. Coll. Cardiol.* **52**, 1024–1032 (2008).
- Woodburn, K. W. *et al.* Phototherapy of cancer and atheromatous plaque with texaphyrins. *J. Clin. Laser Med. Surg.* **14**, 343–348 (1996).
- Overholt, B. F., Panjehpour, M., Denovo, R. C. & Petersen, M. G. Photodynamic therapy for esophageal cancer using a 180° windowed esophageal balloon. *Lasers Surg. Med.* **14**, 27–33 (2005).
- Sum, S., Madden, S., Hendricks, M., Chartier, S. & Muller, J. Near-infrared spectroscopy for the detection of lipid core coronary plaques. *Curr. Cardiovasc. Imaging Rep.* **2**, 307–315 (2009).
- Waxman, S. *et al.* In vivo validation of a catheter-based near-infrared spectroscopy system for detection of lipid core coronary plaques: Initial results of the SPECTACL study. *J. Am. Coll. Cardiol. Imaging* **2**, 858–868 (2009).
- Waxman, S. Near-infrared spectroscopy for plaque characterization. *J. Interv. Cardiol.* **21**, 452–458 (2008).
- Corazza, A. V., Jorge, J., Kurachi, C. & Bagnato, V. S. Photobiomodulation on the angiogenesis of skin wounds in rats using different light sources. *Photomed. Laser Surg.* **25**, 102–106 (2007).
- Wong-Riley, M. T. T. *et al.* Photobiomodulation directly benefits primary neurons functionally inactivated by toxins. *J. Biol. Chem.* **280**, 4761–4771 (2005).
- Vinck, E. M., Cagnie, B. J., Cornelissen, M. J., Declercq, H. A. & Cambier, D. C. Increased fibroblast proliferation induced by light emitting diode and low power laser irradiation. *Lasers Med. Sci.* **18**, 95–99 (2003).

37. Schindl, A. *et al.* Direct stimulatory effect of low-intensity 670-nm laser irradiation on human endothelial cell proliferation. *Br. J. Dermatol.* **148**, 334–336 (2003).
38. Amir, A. *et al.* The influence of helium–neon irradiation on the viability of skin flaps in the rat. *Br. J. Plast. Surg.* **53**, 58–62 (2000).
39. Yao, J. *et al.* Functional nanostructured plasmonic materials. *Adv. Mater.* **22**, 1102–1110 (2010).
40. Yao, J. *et al.* Seeing molecules by eye: Surface plasmon resonance imaging at visible wavelengths with high spatial resolution and submonolayer sensitivity. *Angew. Chem.* **47**, 5013–5017 (2008).

Acknowledgements

We thank T. Banks for help with processing using facilities at the Frederick Seitz Materials Research Laboratory, J. D. Sulkin for help with luminance–current–voltage measurement, H.-S. Kim for discussions and C. Conway and D. Stevenson for help with photography. We also thank Georgios A. Bertos, Ph.D., Sr R&D Principal Engineer Technology Resources Engineering, Baxter Healthcare Corporation, for discussions. This material is based on work supported by Ford Motor Company, the National Science Foundation under grant DMI-0328162 and the US Department of Energy, Division of Materials Sciences, under Award No. DE-FG02-07ER46471, through the Materials Research Laboratory and Center for Microanalysis of Materials (DE-FG02-07ER46453) at the University of Illinois at Urbana-Champaign. R-H.K. would like to thank Samsung

Electronics for doctoral fellowships. J.A.R. acknowledges support from a National Security Science and Engineering Faculty Fellowship from the Department of Defense. Y.H. acknowledges support from NSF (OISE-1043143 and ECCS-0824129). F.G.O. and D.L.K. acknowledge support from the US Army Research Laboratory and the US Army Research Office under contract number W911 NF-07-1-0618 and by the DARPA-DSO and the NIH P41 Tissue Engineering Resource Center (P41 EB002520). We also thank the NIH P41 Tissue Engineering Resource Center (P41 EB002520) for support of the studies, all of which were conducted under approved animal protocols at Tufts University.

Author contributions

R-H.K., D-H.K., B.H.K., S-I.P. and J.A.R. designed the experiments. R-H.K., D-H.K., B.H.K., J.X., B.P., J.Y., M.L., Z.J.L., A-P.L., D.G.K., F.G.O., Y.H., Z.K. and J.A.R. carried out experiments and analysis. R-H.K., D-H.K., J.X., R.G., J.Y., Y.H., F.G.O., D.L.K. and J.A.R. wrote the paper.

Additional information

The authors declare no competing financial interests. Supplementary information accompanies this paper on www.nature.com/naturematerials. Reprints and permissions information is available online at <http://npg.nature.com/reprintsandpermissions>. Correspondence and requests for materials should be addressed to J.A.R.

Waterproof AlInGaP optoelectronics on stretchable substrates with applications in biomedicine and robotics

Rak-Hwan Kim^{1*}, Dae-Hyeong Kim^{1*}, Jianliang Xiao^{1,2}, Bong Hoon Kim^{1,3}, Sang-Il Park¹, Bruce Panilaitis⁴, Roozbeh Ghaffari⁵, Jimin Yao⁶, Ming Li^{2,7}, Zhuangjian Liu⁸, Viktor Malyarchuk¹, Dae Gon Kim¹, An-Phong Le⁶, Ralph G. Nuzzo⁶, David L. Kaplan⁴, Fiorenzo G. Omenetto⁴, Yonggang Huang², Zhan Kang⁷, John A. Rogers^{1†}

¹*Department of Materials Science and Engineering, Beckman Institute for Advanced Science and Technology and Frederick Seitz Materials Research Laboratory, University of Illinois at Urbana-Champaign, Urbana, IL 61801 USA*

²*Department of Mechanical Engineering and Department of Civil and Environmental Engineering, Northwestern University, Evanston, IL 60208 USA*

³*Department of Materials Science and Engineering, Korea Advanced Institute of Science and Technology (KAIST), 373-1 Guseong-dong, Yuseong-gu, Daejeon, Republic of Korea*

⁴*Department of Biomedical Engineering, Tufts University, Medford, MA 02155, USA*

⁵*MC10 Inc., 36 Cameron Avenue, Cambridge, MA 02140*

⁶*Department of Chemistry, University of Illinois at Urbana-Champaign, Urbana, IL 61801 USA*

⁷*State Key Laboratory of Structural Analysis for Industrial Equipment, Dalian University of Technology, Dalian 116024, China*

⁸*Institute of High Performance Computing, 1 Fusionopolis Way, #16-16 Connexis, Singapore, 138632*

*R.-H. Kim and D.-H. Kim contributed equally.

¹To whom correspondence should be addressed. E-mail: jrogers@uiuc.edu

Supplementary Information

Contact scheme

In this paper, simple metal (Cr/Au) to doped GaAs contacts are used instead of ohmic contacts. For improved electrical characteristics, conventional ohmic contacts of metal interconnects to GaAs can be implemented. To form the ohmic contact, a series of metal stacks followed by appropriate annealing (*n* ohmic contact metals: Pd/Ge/Au followed by anneal at 175 °C for 1 hour, *p* ohmic contact metal: Pt/Ti/Pt/Au in this paper) can be used, which results in lower take-off voltage can be obtained as shown in Fig. S22a.

Long-term operation

Long-term operation test using two LED devices, connected in series, on a thin slab of PDMS was performed under the constant current mode (0.75 mA). Both devices showed robust and reliable performance during the continuous operation for 100 hours without affecting I-V characteristics as shown in Fig. S22b.

FEM simulation of balloon deformation

Figure S23a illustrates the mechanics model for inflating and transfer printing onto the PDMS balloon of Fig. 1. The initially flat, circular thin film (initial state, upper left frame of Fig. S8a) of radius r is fixed at its outer boundary, and is inflated by air to a spherical cap of height h (inflated state, right frame of Fig. S23a). The radius of the sphere is $R = (h^2 + r^2)/(2h)$. The spherical cap is pressed down and flattened during

transfer printing, as shown in the lower left frame of Fig. S23a (as-print state). The deformation is uniform along the meridional direction during inflation, while all material points move vertically downward during printing. Therefore, for a point of distance x_0 to the film center at the initial state, its position changes to x_1 in the inflated state with an arc distance s_1 to the film center, and then changes to x_2 in the state during printing, where $s_1 = (Rx_0/r)\arcsin(r/R)$ and $x_1 = x_2 = R\sin[(x_0/r)\sin^{-1}(r/R)]$.

These give the meridional and circumferential strains of the inflated state as

$$\varepsilon_{\theta 1} = \frac{R}{r} \arcsin \frac{r}{R} - 1, \quad (\text{S1})$$

$$\varepsilon_{\varphi 1} = \frac{R}{x_0} \sin \left(\frac{x_0}{r} \arcsin \frac{r}{R} \right) - 1. \quad (\text{S2})$$

The meridional and circumferential strains at the state during printing are given by

$$\varepsilon_{\theta 2} = \frac{R}{r} \cos \left(\frac{x_0}{r} \sin^{-1} \frac{r}{R} \right) \sin^{-1} \frac{r}{R} - 1, \quad (\text{S3})$$

$$\varepsilon_{\varphi 2} = \frac{R}{x_0} \sin \left(\frac{x_0}{r} \sin^{-1} \frac{r}{R} \right) - 1. \quad (\text{S4})$$

Finite element method (FEM) was used to study this process in order to validate the analytical model above. The contours of meridional and circumferential strains of the inflated state appear in the upper and lower left frames of Fig. S23b, respectively. The results are compared with analytical solutions Eqs. (S1) and (S2) in the right frame of Fig. S23b, and show good agreement. Therefore, the analytical formulae, Eqs. (S1) and (S2), can be used to predict the PDMS strain under different inflation, and further to estimate the strain in devices on the balloon surface. Figure S23c shows the contours of meridional (upper left frame) and circumferential (lower left frame) strains of the as-print state, and the comparison with analytical solutions from Eqs. (S3) and (S4) (right

frame). The analytical solutions, once again, agree well with FEM simulations without any parameter fitting.

Bending of LEDs on various substrates

The LED, as illustrated in Fig. S24, consists of multiple layers with thicknesses $h_1=3.5$ um, $h_2=2.5$ um, $h_3=1.2$ um and $h_4=1.2$ um, and Young's moduli are $E_{SU8}=5.6$ GPa, $E_{GaAs}=85.5$ GPa and $E_{PI}=3.2$ GPa. These layers are modeled as a composite beam with equivalent tensile and bending stiffnesses. The PDMS strain isolation layer has thickness $h_5=50$ um and Young's modulus $E_{PDMS}=0.4$ MPa. The Young's modulus E_{sub} and thickness H of the substrate are 1.2 MPa and 0.8 mm for the fabric, 23.5 MPa and 0.5 mm for the fallen leaf, and 600 MPa and 0.2 mm for the paper. The strain isolation model [11] then gives very small maximum strains in GaAs, 0.043%, 0.082% and 0.23% for the completely folded fabric, leaf and paper, respectively. The minimal bend radii are the same as the corresponding substrate thicknesses H , i.e., 800 μ m, 500 μ m and 200 μ m for the fabric, leaf and paper, respectively. For the Al foil substrate, the minimum bend radius is obtained as 139 μ m when the strain in GaAs reaches 1%.

Without the PDMS strain isolation layer, the LED and substrate are modeled as a composite beam. The position of neutral axis (measured from the top surface) is given by

$$y_0 = \frac{\left\{ E_{SU8} \left[(h_1 + h_3)^2 + 2h_2h_3 \right] + E_{PI}h_4(2h_1 + 2h_2 + 2h_3 + h_4) \right\} + E_{GaAs}h_2(2h_1 + h_2) + E_{sub}H(2h_1 + 2h_2 + 2h_3 + 2h_4 + H)}{2 \left[E_{SU8}(h_1 + h_3) + E_{GaAs}h_2 + E_{PI}h_4 + E_{sub}H \right]}.$$

The maximum strain in GaAs is $\varepsilon_{GaAs} = \frac{1}{R_b} \max(|y_0 - h_1|, |h_1 + h_2 - y_0|)$, where R_b is the bending radius. Therefore, the minimum bending radius of LED array on the substrate

is $R_b = \frac{1}{\varepsilon_{failure}} \min(|y_0 - h_1|, |h_1 + h_2 - y_0|)$, where $\varepsilon_{failure} = 1\%$ is the failure strain of GaAs.

For the fabric substrate, the maximum strain in GaAs is only 0.34% even when it is completely folded, which gives the minimum bending radius the same as the thickness 0.8 mm. For the fallen leaf and the paper, the minimum bending radii are 1.3 mm and 3.5 mm.

SI Figure Legends

Figure S1. Schematic illustration of epitaxial layer (a) and fabrication processes for μ -ILEDs arrays on a carrier glass substrate after transfer printing (b).

Figure S2. (a) Schematic illustration (left frame) and corresponding microscope (top right frame) and SEM (bottom right frame) images of a 6×6 μ -ILEDs on a handle glass substrate coated with layers of polymers (epoxy / PI / PMMA). (b) Schematic illustration (left frame) and corresponding microscope (top right frame) and optical (bottom right frame) images of a 6×6 μ -ILEDs array which is picked up with a PDMS stamp for transfer printing. A shadow mask for selective deposition of Cr/SiO₂ (thickness: 3nm/30nm) covers the retrieved array on a soft elastomeric PDMS stamp. (c) Schematic illustration of transfer printing to a pre-strained thin (thickness: ~ 400 μ m) PDMS substrate (left frame) and microscope (top right frame) and SEM (bottom right frame) images of the transferred μ -ILEDs array on a prestrained thin PDMS substrate. Prestrain value was $\sim 20\%$.

Figure S3. (a) Schematic illustration of top encapsulation layers indicating some of the key dimensions. (b) Schematic illustration of the cross sectional structure at an island, with approximate thicknesses for each layer. The inset corresponds to an SEM image of a μ -ILEDs array after transfer printing to a thin PDMS substrate with prestrain of $\sim 20\%$. (c) Schematic illustration of the cross sectional structure at metal interconnection bridges, with approximate thicknesses of each layer.

Figure S4. (a) Tilted view SEM images of adjacent μ -ILEDs (yellow dashed boxes) before (left, formed with $\sim 20\%$ pre-strain) and after (right) stretching along the horizontal direction (red arrows). (b) Strain distributions determined by 3D-FEM for the cases corresponding to frames in (a). The black outlines indicate the positions of the devices and the serpentines before relaxing the pre-strain.

Figure S5. (a) Optical microscope images of two pixels in a μ -ILEDs array with a serpentine bridge design before (left frame) and after (right frame) external stretching along the horizontal direction. The upper and lower images show optical micrographs in emission light off (upper) and on (lower) states. The distance between adjacent pixels appears in the lower images and used for calculation of applied strains. The lower images were obtained without external illumination. (b) Optical micrograph images of two pixels in a μ -ILEDs array before (left frame) and after (right frame) external stretching along the diagonal direction. (c) FEM simulation under external stretching along the diagonal direction (left frame), and strain contours in the GaAs active island (top right frame) and the metal bridge (bottom right frame).

Figure S6. Optical images of a 6×6 μ -ILEDs array with a serpentine mesh design with external illumination under the same strain circumstances as Fig. 1b.

Figure S7. (a) Optical image of an 8×8 μ -ILEDs array on a thin PDMS substrate in its on state, which is under the same kind of deformed condition as bottom left frame of Fig. 1d. (b) Top view optical images of same array as Fig. 1d in its ‘flat’ (left frame) and ‘inflated’ state (right frame) without external illumination. (c) Spatial distribution of FEM results of the right frame of Fig. 1d and analytical solutions calculated from Eqs. (S1) and (S2).

Figure S8. (a) Schematic illustrations of a 3×8 μ -ILEDs array integrated on a thin PDMS substrate with detailed dimensions (upper frame: registrations of the μ -ILEDs on a PDMS donor substrate, lower frame: entire view of the printed 3×8 μ -ILEDs array). The inset on top represents an optical microscope image of this μ -ILEDs array on a handle glass substrate before transfer printing. (b) Magnified view of the SEM image in Fig. 2b. The white dotted rectangle highlights the non-coplanar bridge structures. (c) Voltage at 20 μ A current for each twisting cycle of 360° .

Figure S9. FEM strain contours of axial (top), width (center), and shear (bottom) strains for 360° twisted PDMS substrate.

Figure S10. Fatigue test result of a 6×6 μ -ILEDs array as shown in Fig. 2e. (a) Plot of I-V characteristics of a 6×6 μ -ILEDs array as a function of deformation cycles. (b) Plot

of voltage needed to generate a current of 20 μA measured after deformation cycles up to 1000 times. Each deformed state is approximately same as shown in Fig. 2e

Figure S11. (a) Schematic illustration of stacked devices describing states of Fig. 3b. (b) Optical images of stacked devices as shown in Fig. 3b, collected without external illumination.

Figure S12. (a) The strain distribution of the two-layer system in the stacked array bent to a radius of curvature 2 mm, as shown in Fig. 3c. The black dashed rectangles demonstrate the positions of μ -ILEDs. (b) The strain distribution in GaAs layers in the μ -ILEDs island.

Figure S13. (a) Optical image of a 6×6 μ -ILEDs array with serpentine metal interconnects, integrated on fabrics, in its bent and on state (bending radius ~ 4.0 mm). The inset shows the device in its flat and off state. (b) Plot of I-V characteristics of this array in its bent state. Inset provides a graph of the voltage needed to generate a current of 20 μA , measured after different numbers of cycles of bending deformation. (c) Optical image of an 8×8 μ -ILEDs array with a human pattern, integrated on a fallen leaf, in its bent and on state. The inset image was collected with external illumination. (d) Plot of I-V characteristics in the bent state as shown in Fig. S13c. (e) Optical image of a μ -ILEDs array integrated on a paper in its folded and on state. (f) Optical image of the same μ -ILEDs array as shown in Fig. 3e in its mildly crumbled state. Inset represents microscope image of adjacent four pixels in their on states.

Figure S14. (a) Plot of I-V characteristics of a 6×6 μ -ILEDs array integrated on paper in its flat (Fig. 3d inset) and folded (Fig. 3d) state. (b) Plot of I-V characteristics of a 6×6 μ -ILEDs array integrated on aluminum foil in its flat (Fig. 3e inset) and crumpled (the center frame of Fig. 3e) state. (c) Fatigue tests of arrays of 6×6 μ -ILEDs as shown in Fig. S13e. Plot of I-V characteristics of a μ -ILEDs array integrated on paper as a function of deformation cycles (left frame). Plot of voltage needed to generate a current of $20 \mu\text{A}$ measured after deformation cycles up to 1000 times (right frame). (d) Fatigue tests of arrays of 6×6 μ -ILEDs as shown in Fig. S13f. Plot of I-V characteristics of a μ -ILEDs array integrated on aluminum foil as a function of deformation cycles (left frame). Plot of voltage needed to generate a current of $20 \mu\text{A}$ measured after deformation cycles up to 1000 times (right frame).

Figure S15. SEM images of various substrate such as fabrics (a), Al foils (b), paper (c), and fallen leaves (d) before (left frame) and after (right frame) coating of thin layer of PDMS.

Figure S16. Optical image of single μ -ILED with long straight interconnects, integrated on a flexible thread with diameter of diameter $\sim 2.5 \text{ mm}$ (a), and diameter $\sim 0.7 \text{ mm}$ (b), respectively. (c) Optical image of a single LED device with long interconnects, integrated on $\sim 300 \mu\text{m}$ -wide threads in its bent and un-deformed (inset) states, respectively. (d) Schematic illustration describing ‘rolling method’. (e) Optical image of a 4×6 μ -ILEDs array with serpentine bridge interconnects integrated on a glass tube using a rolling method for printing. (f) The suture demonstration using μ -ILEDs array

mounted on a thread for radiation therapy with an incision in paper (thread diameter ~700 μm).

Figure S17. Schematic illustration of the encapsulation of an implantable array of μ -ILEDs as described in Figs. 4b and c.

Figure S18. (a) Light intensity spectrum of single μ -ILED, measured with conventional spectrometer (Ocean Optics, USA). (b) Percent transmittance spectrum through plasmonic nanohole array, measured with conventional spectrometer (CARY, Varian, USA). (c) Transmitted light intensity spectrum through plasmonic nanohole array at the relevant wavelength range, calculated by multiplying single LED intensity in (a) and % transmittance in (b).

Figure S19. (a) Measurement results from a representative sensor (top), operated while integrated with a tube, as a sequence of aqueous solutions of PEG (polyethylene glycol) pass through. (b) The percentage increase in light transmitted from the μ -ILED, through the plasmonic crystal and measured on the opposite side of the tube with a silicon photodiode, as a function of PEG concentration. (c) Refractive indexes change with different glucose and PEG concentrations.

Figure S20. (a) Plot of I-V characteristics of photodiodes at different distances between an optical proximity sensor and an approaching object as explained in Figs. 6a-c. (b) Plot of I-V characteristics of 2nd layer (an array of photodiode) as a function of the current level of 1st layer (an array of μ -ILEDs) under negative bias in the stacked device.

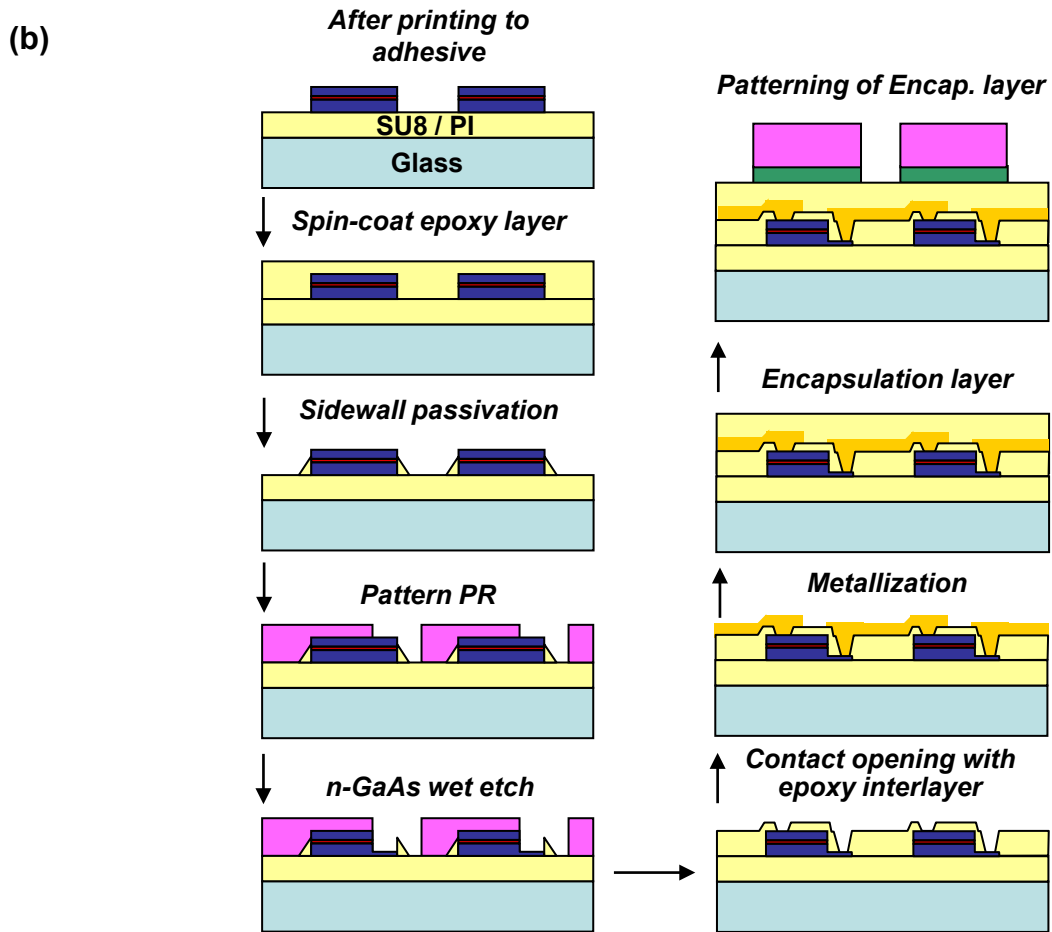
(c) Plot of photocurrent of an array of 6×6 μ -PDs that is stacked on the layer of a 6×6 μ -ILEDs array as a function of operation current of μ -ILEDs in the stacked device. (d) Plot of current-voltage characteristics of an array of 6×6 photodiodes as a function of distance between the device and the approaching object in the stacked device. Voltage range of an array of 6×6 μ -PDs was from 0 V to -10 V during the 6×6 μ -ILEDs array was in emission light up state (operation current of μ -ILEDs array: 3 mA). (e) Re-plotting of Fig. S20d as a function of distance between approaching object and μ -PDs.

Figure S21. IV characteristics of the same μ -ILEDs array as shown in Fig. 6c at different immersion times.

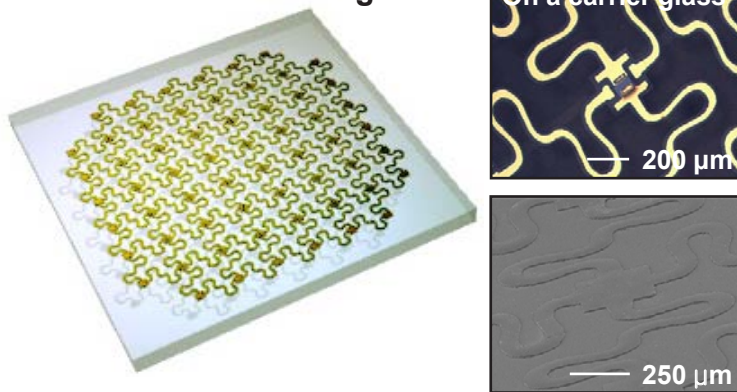
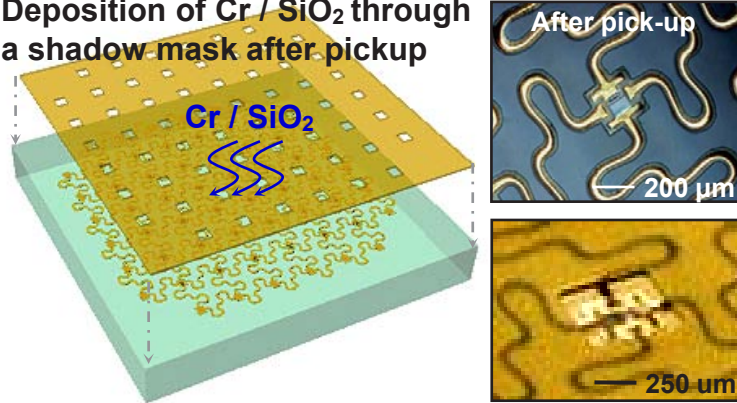
Figure S22. (a) Result of Luminance (L) – Current (I) – Voltage (V) measurement of an individual pixel with and without applied ohmic contacts. (b) Applied voltage to generate a current of 20 μ A, measured after different operation time. The inset provides I-V characteristics with different operation time.

Figure S23. (a) Schematic illustration of analytical model for the inflation and printing-down of PDMS film. (b) FEM contours of meridional (upper left) and circumferential (lower left) strains of the inflated state and its comparison with analytical solutions calculated from Eqs. (1) and (2). (c) FEM contours of meridional (upper left) and circumferential (lower left) strains of the as-printed state and its comparison with analytical solutions Eqs. (S3) and (S4) (right frame).

Figure S24. Schematic illustration of the cross section of μ -ILEDs on a substrate

**Figure S1**

(a) Device fabrication on a glass

(b) Deposition of Cr / SiO₂ through a shadow mask after pickup

(c) Transfer printing

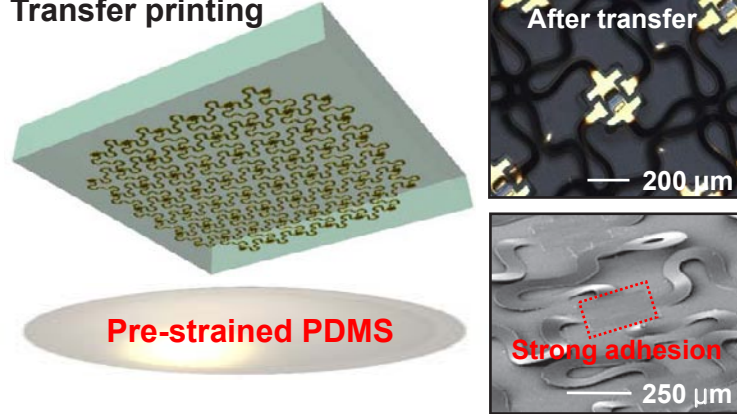


Figure S2

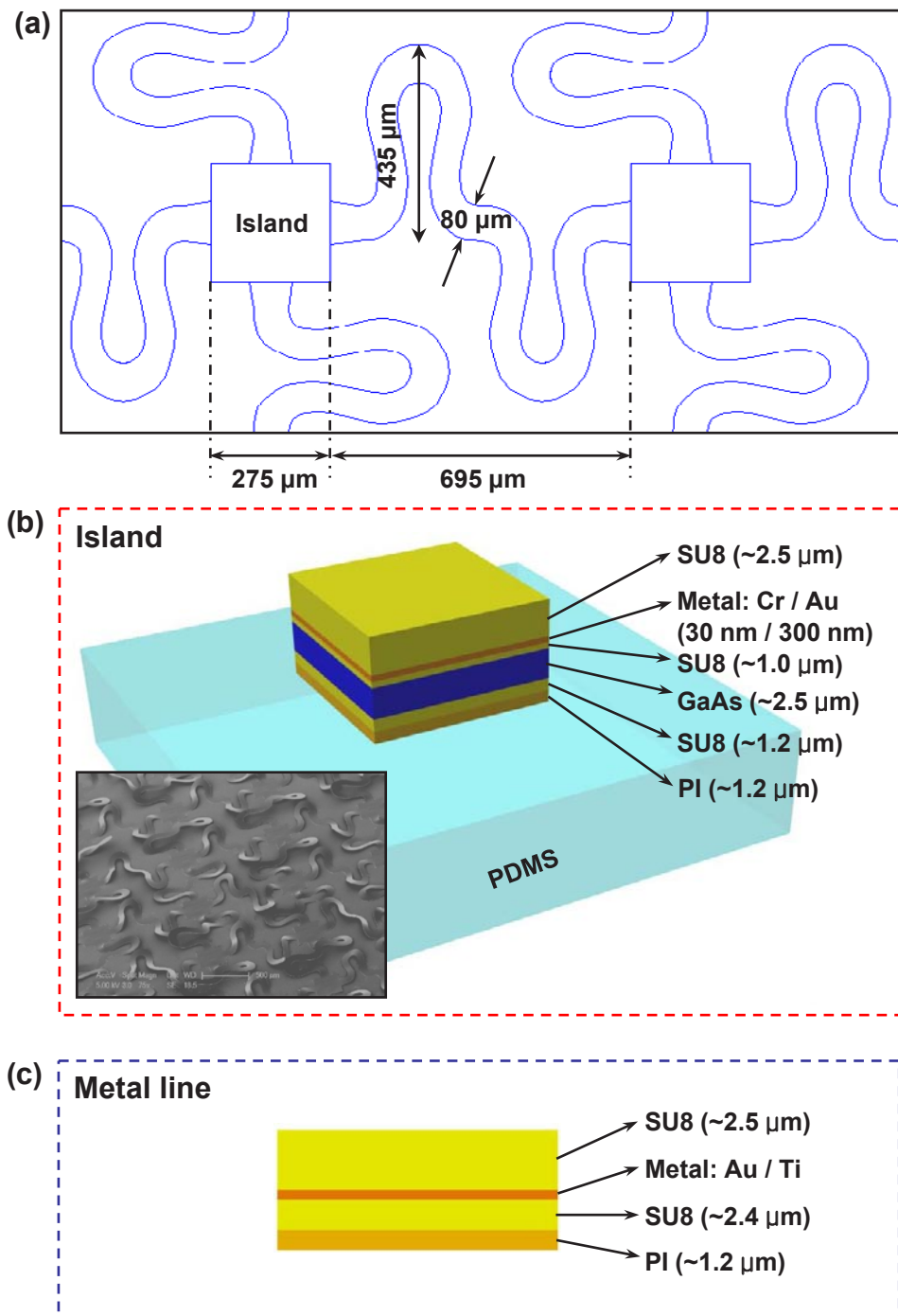
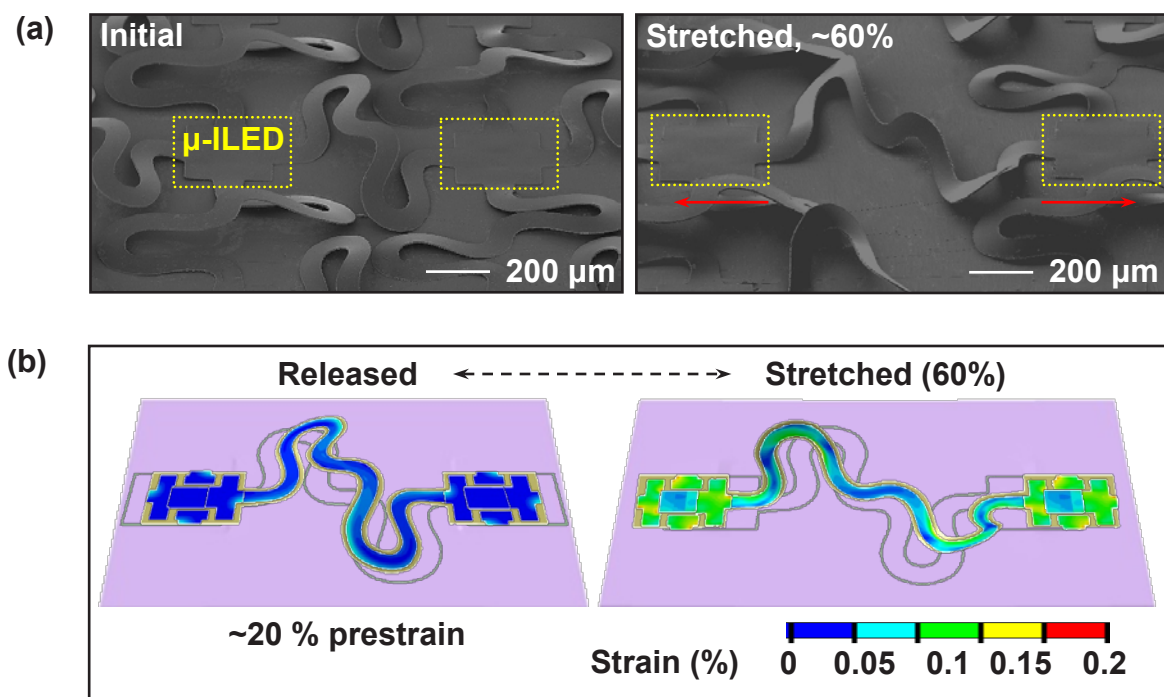


Figure S3

**Figure S4**

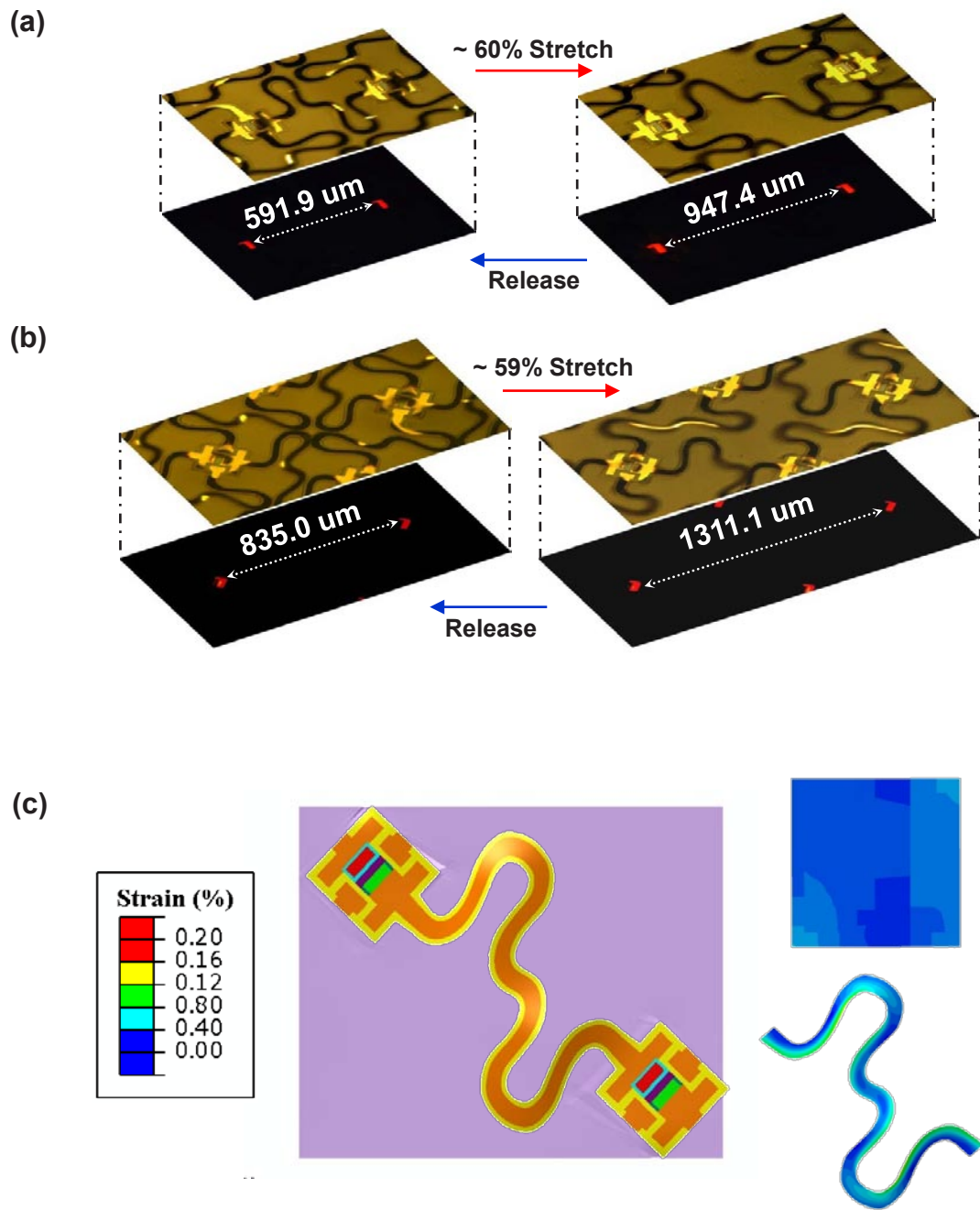


Figure S5

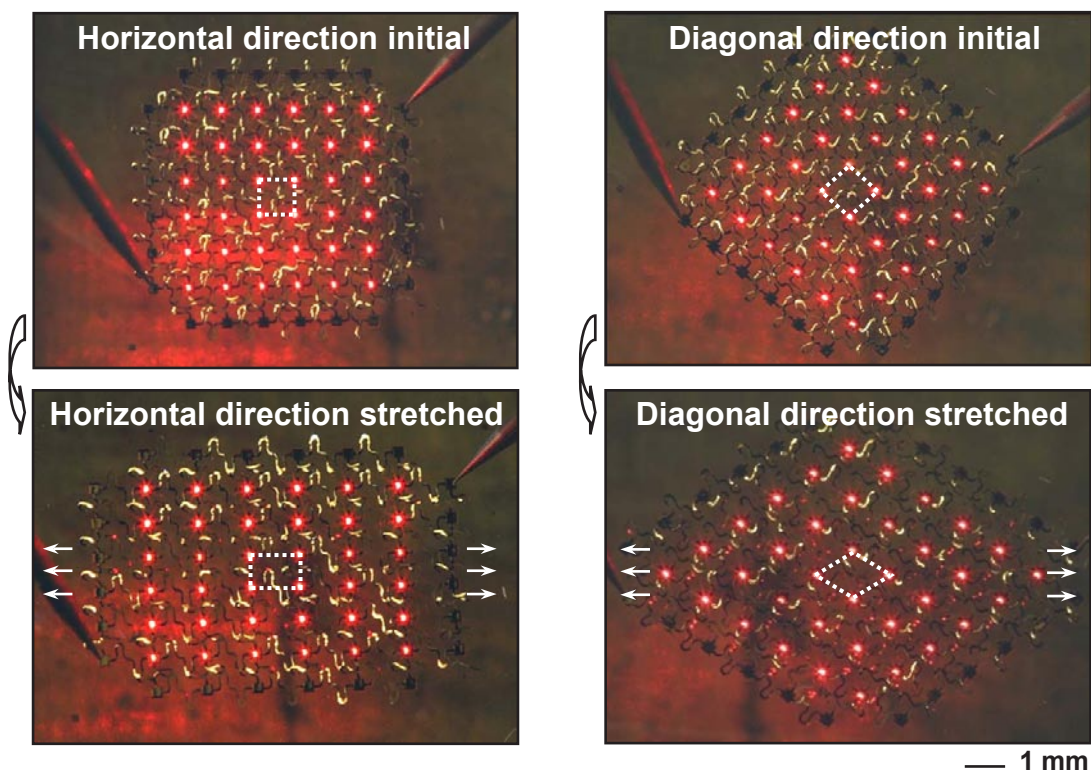
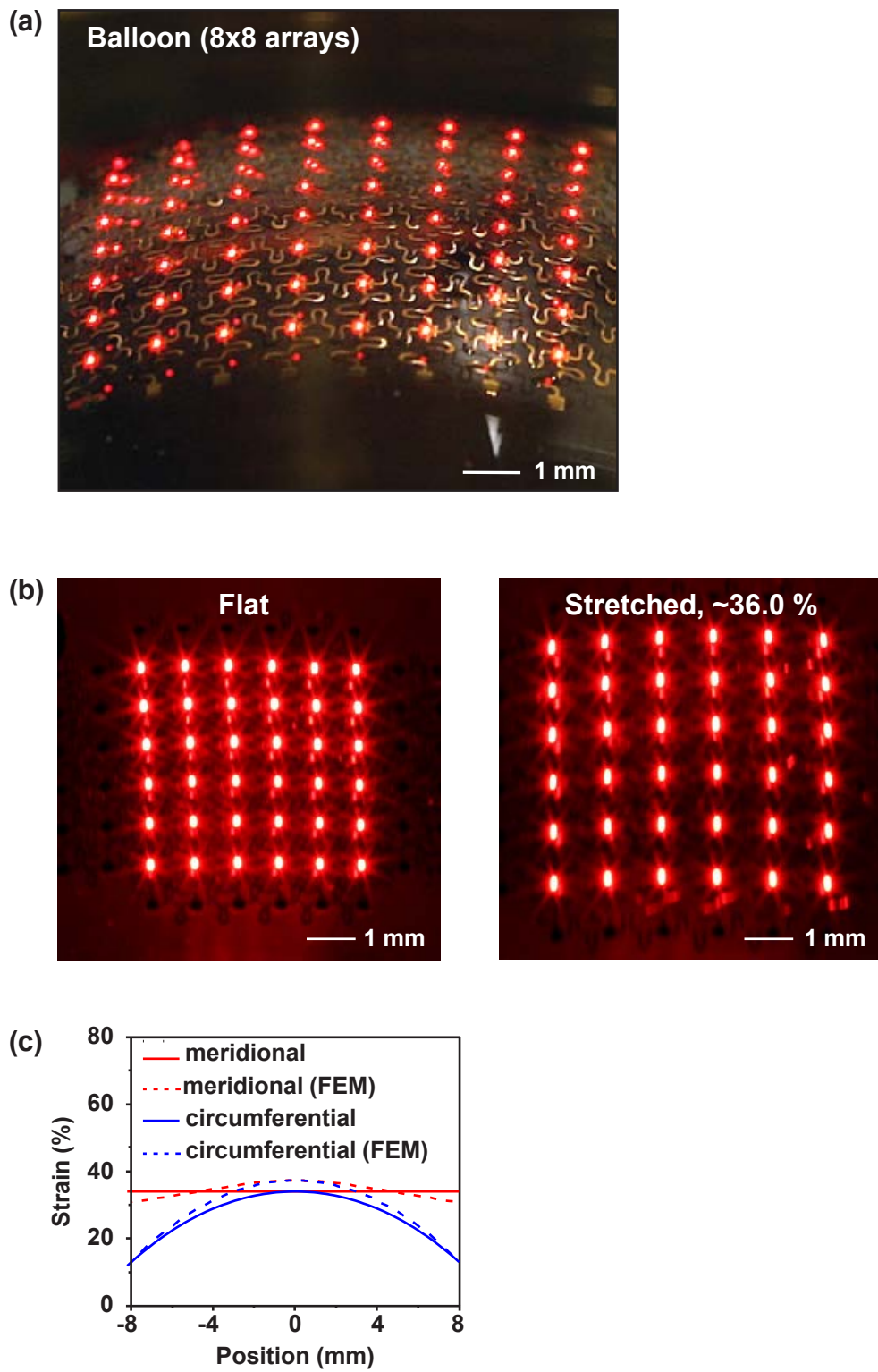


Figure S6

**Figure S7**

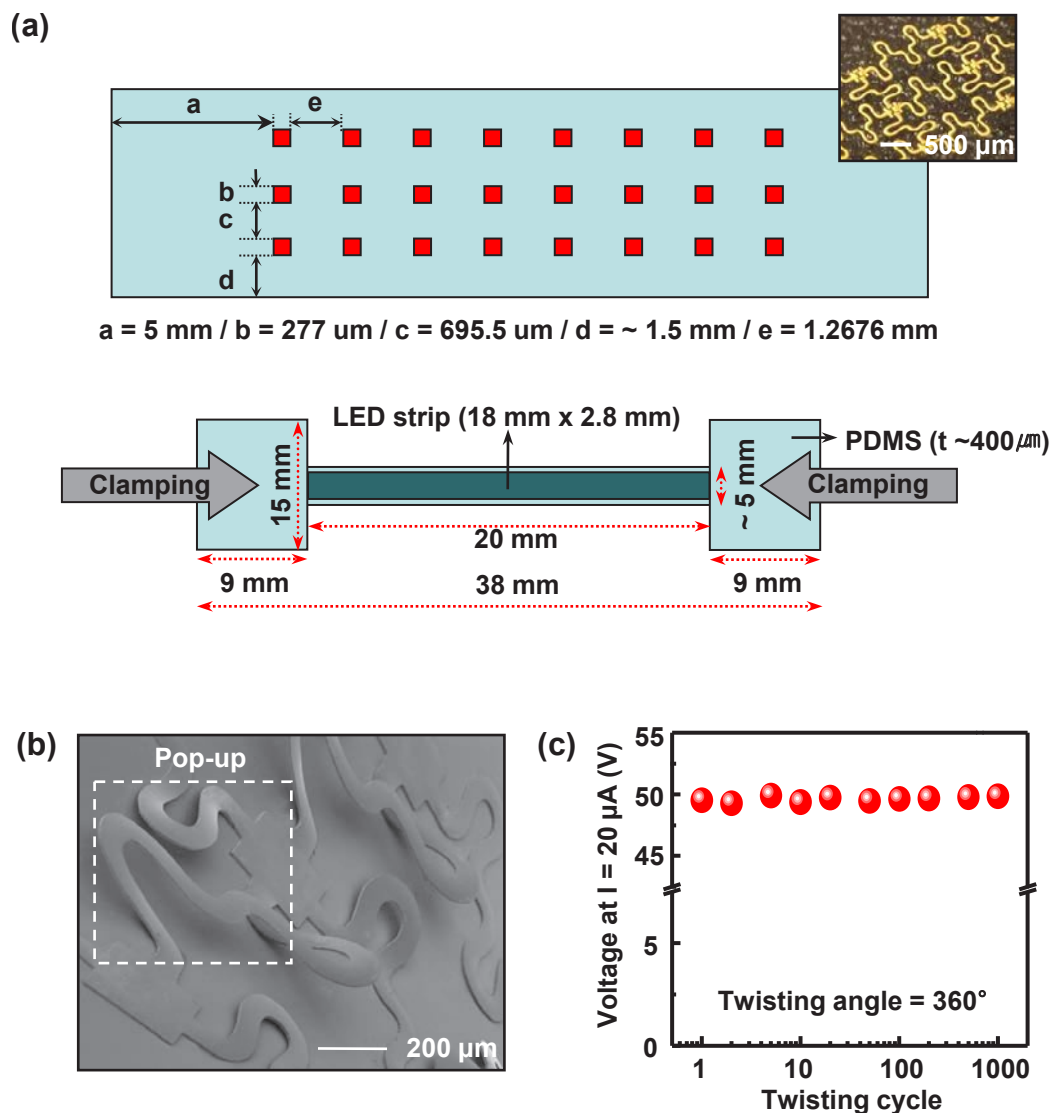
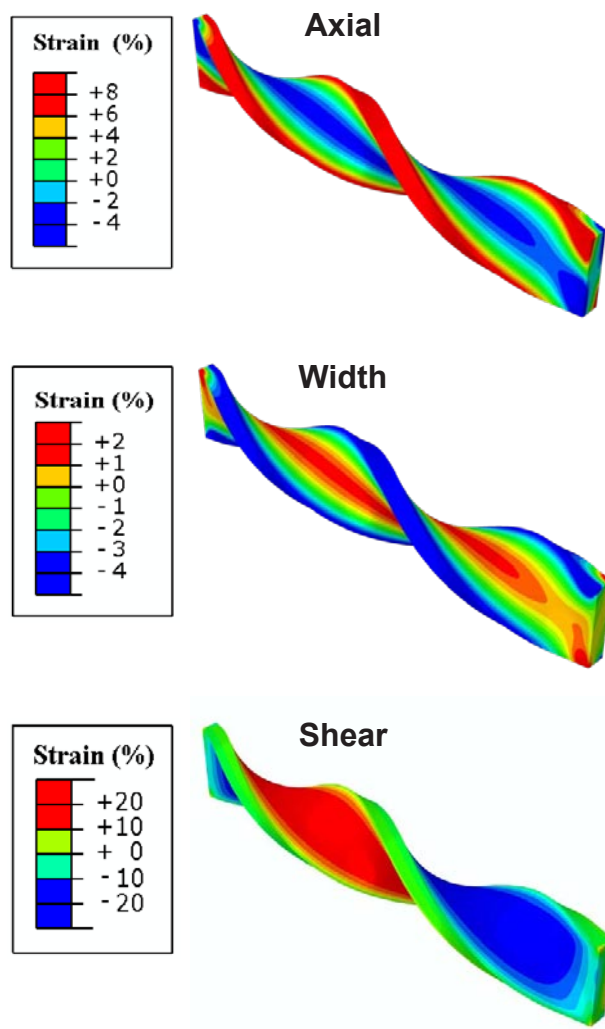


Figure S8

**Figure S9**

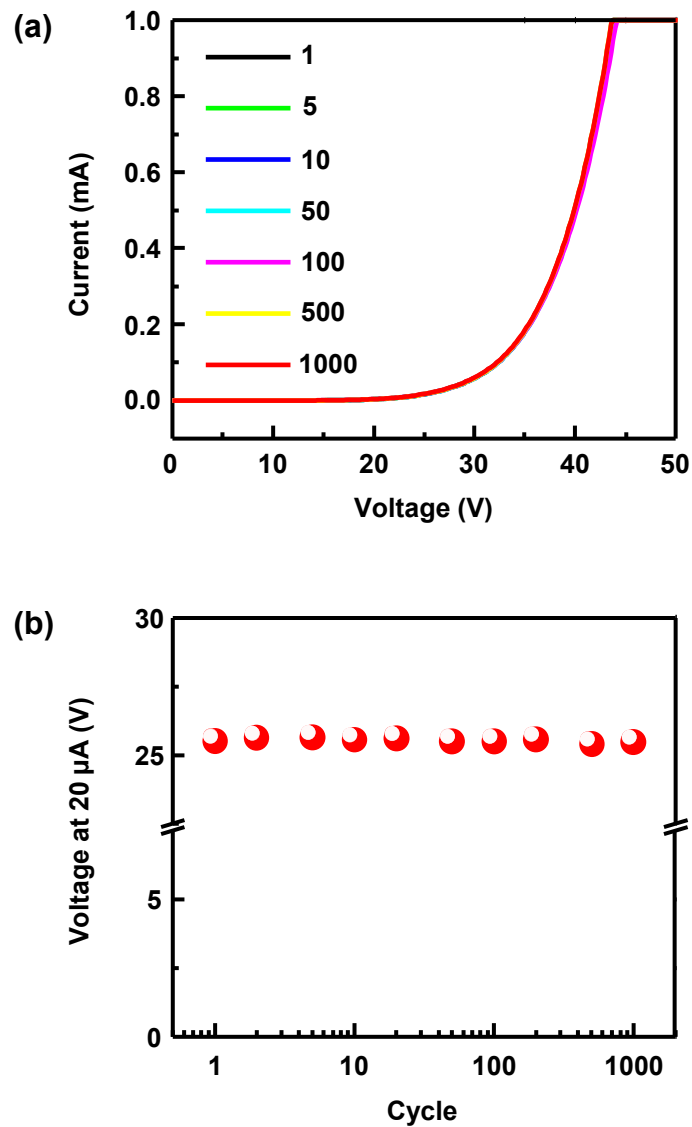


Figure S10

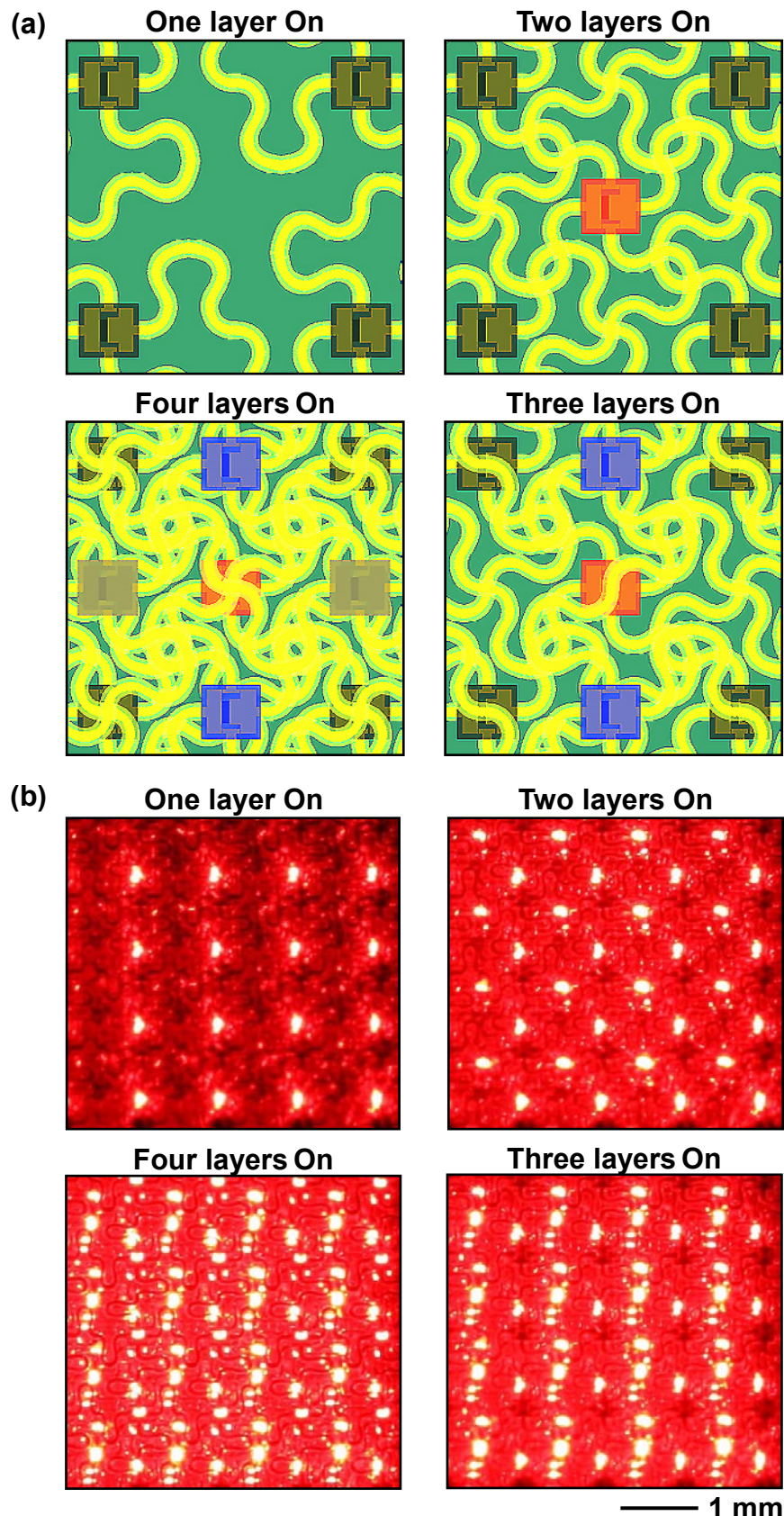
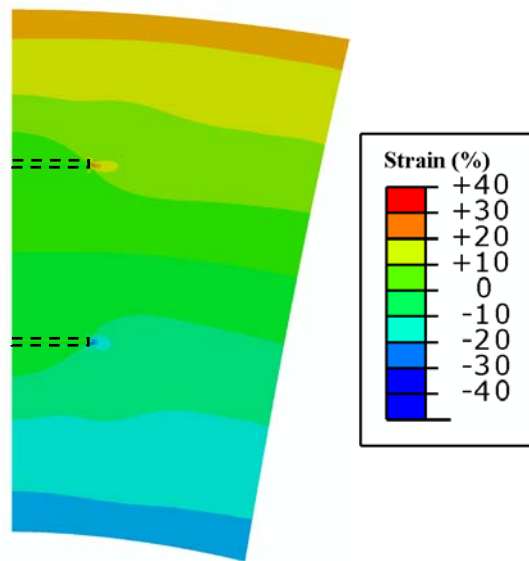


Figure S11

(a)



(b)

**Figure S12**

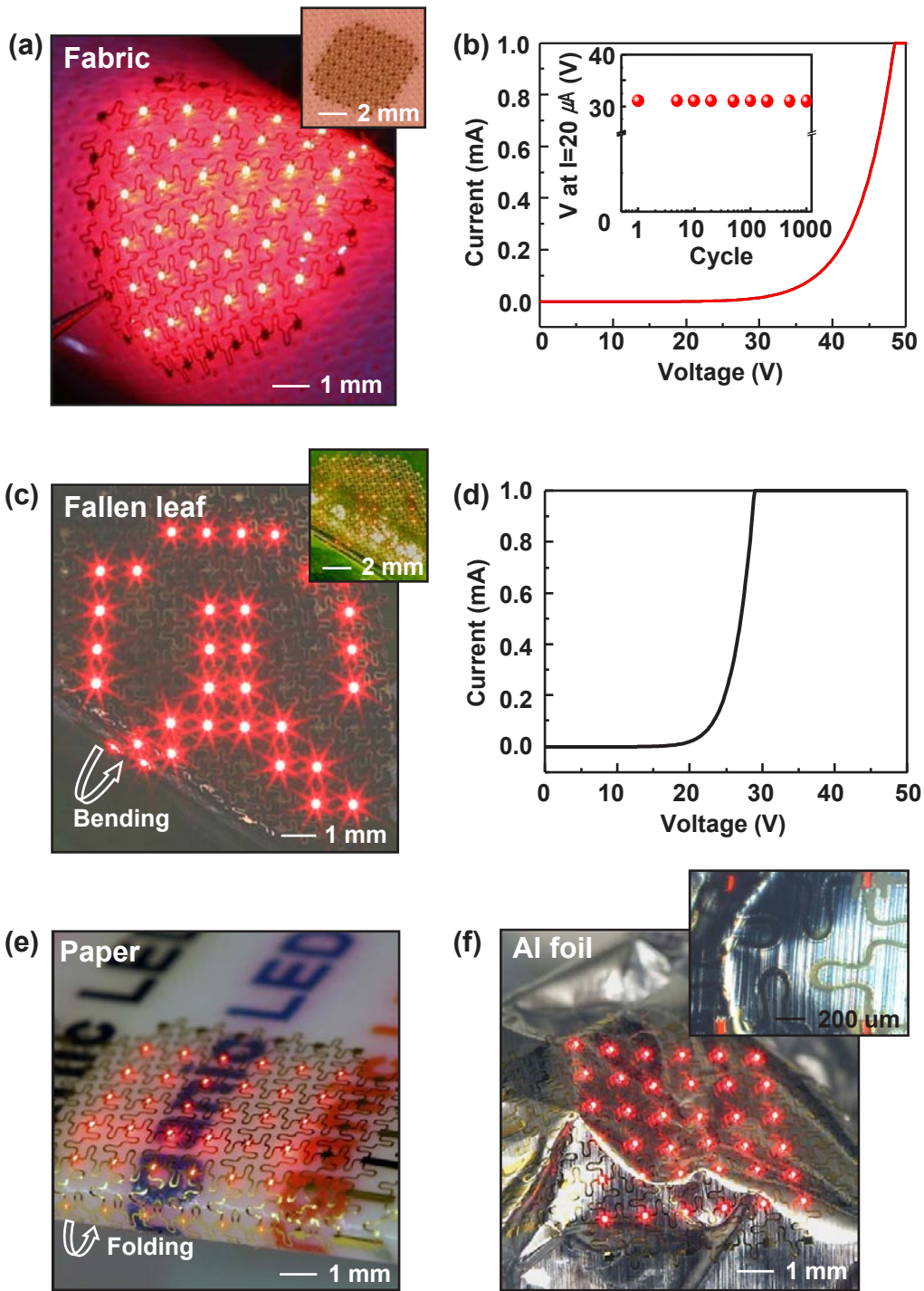


Figure S13

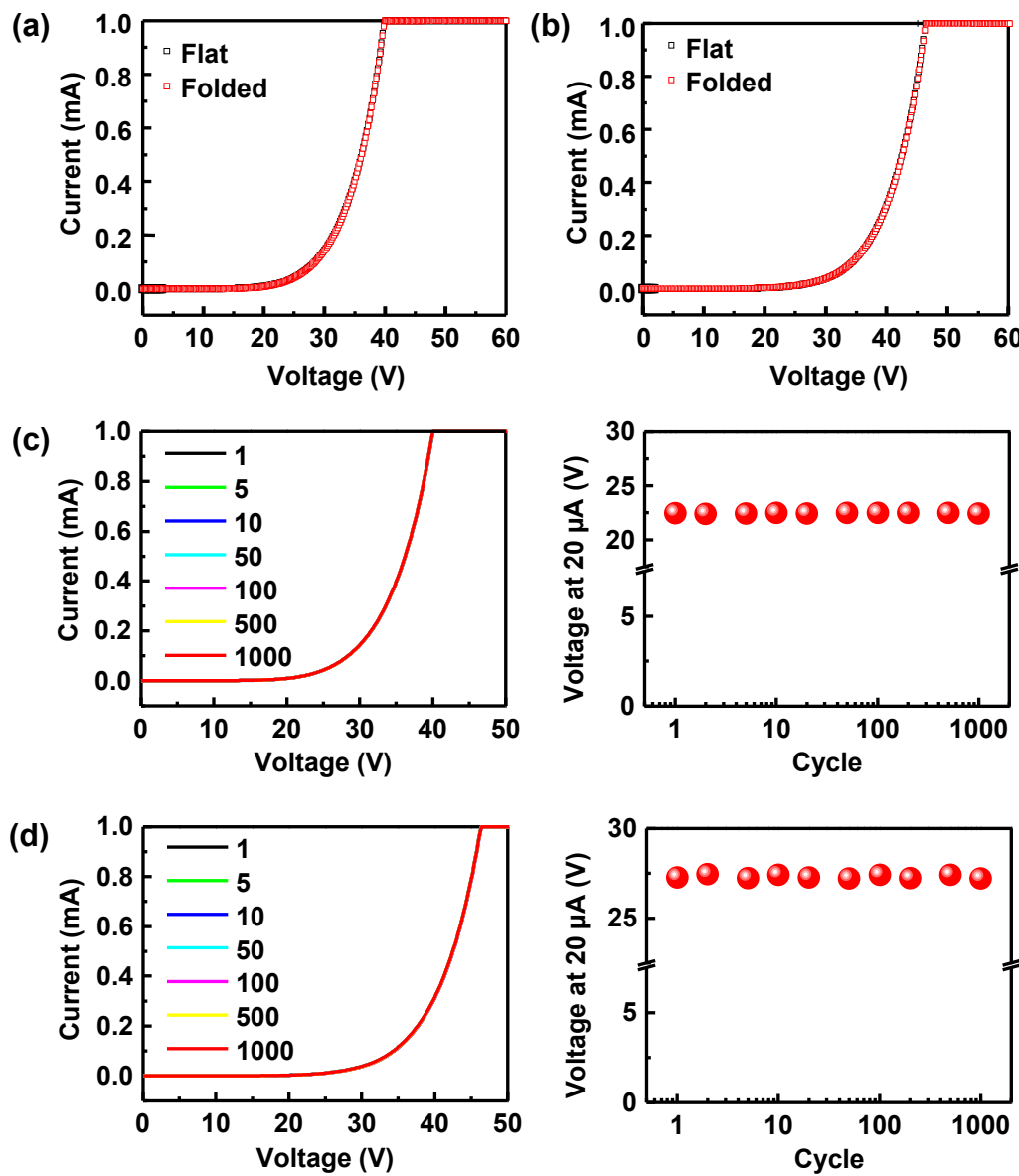


Figure S14

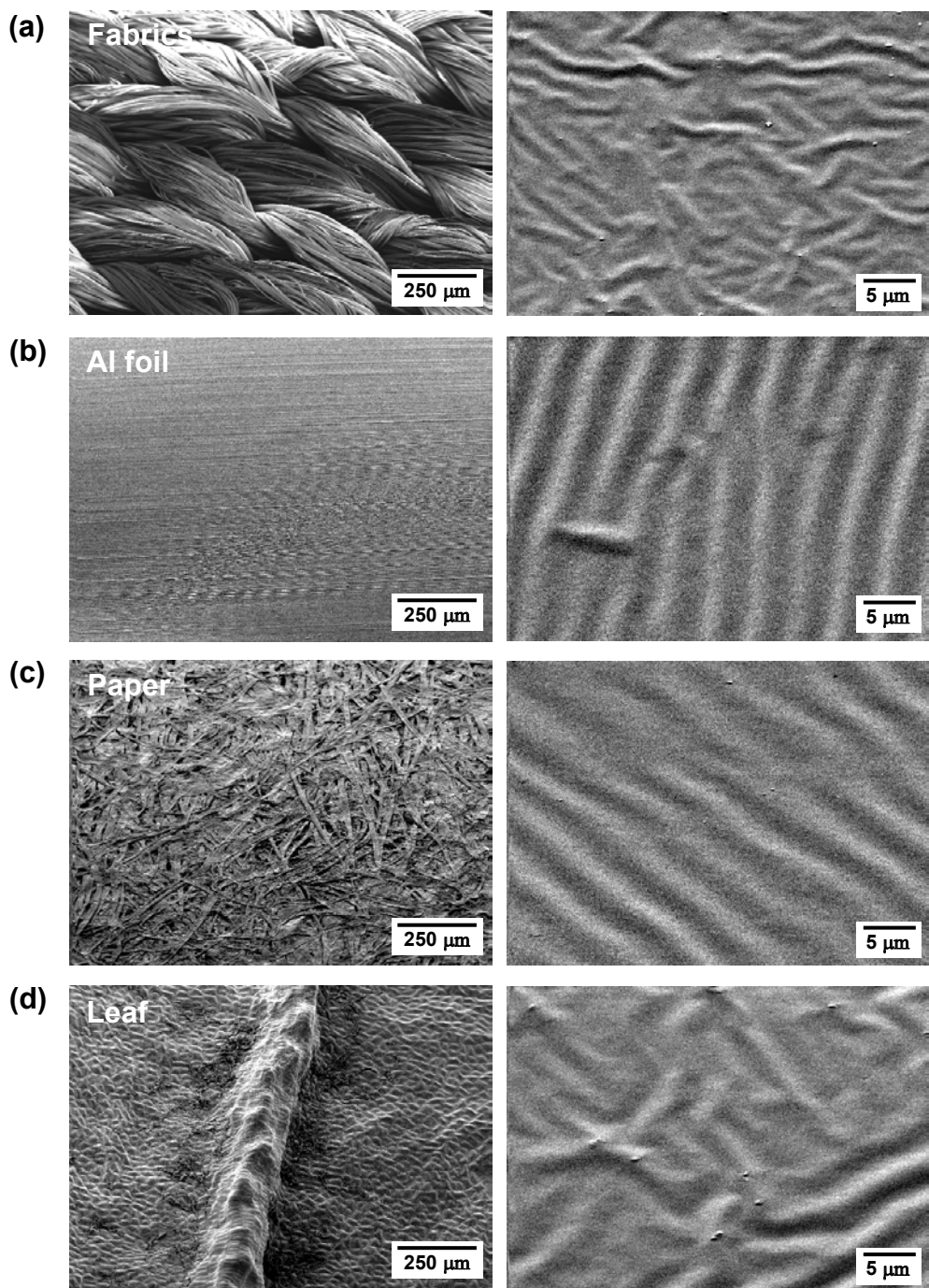


Figure S15

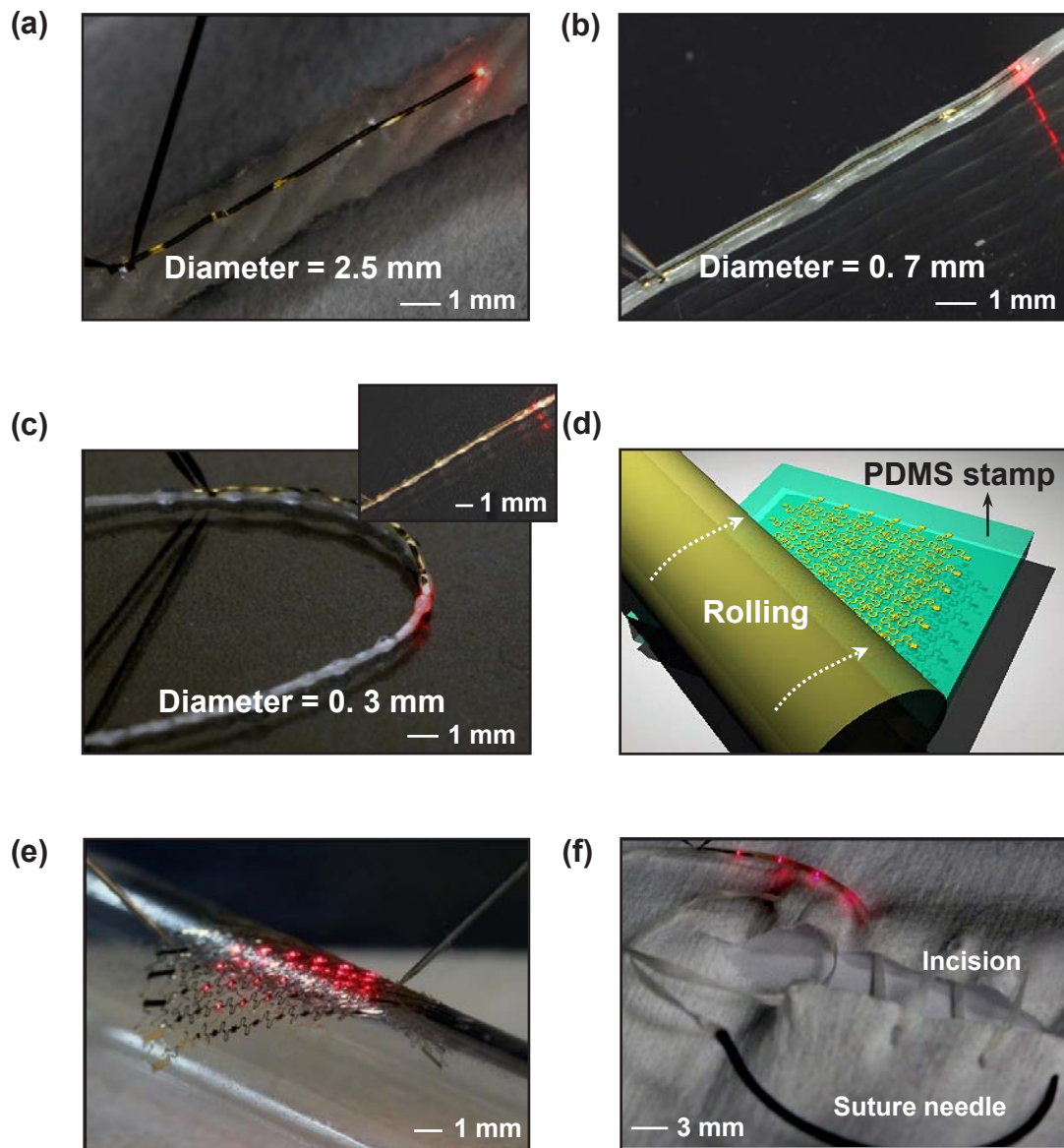
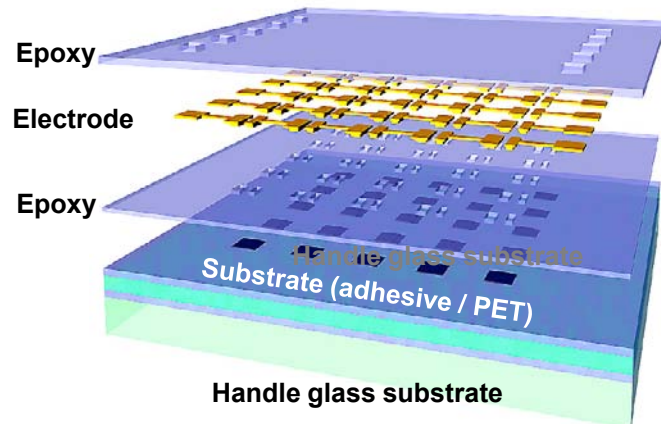
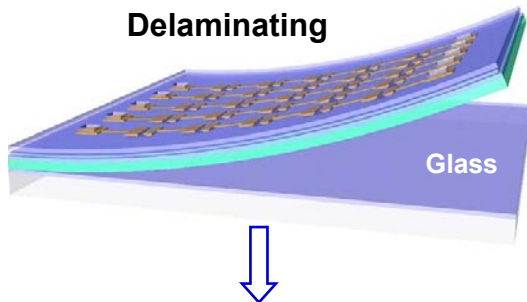
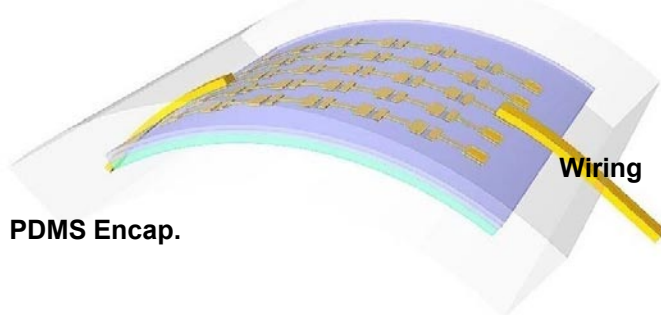


Figure S16

Process on handle substrate**Delaminating****Wiring & Encap. with PDMS****Figure S17**

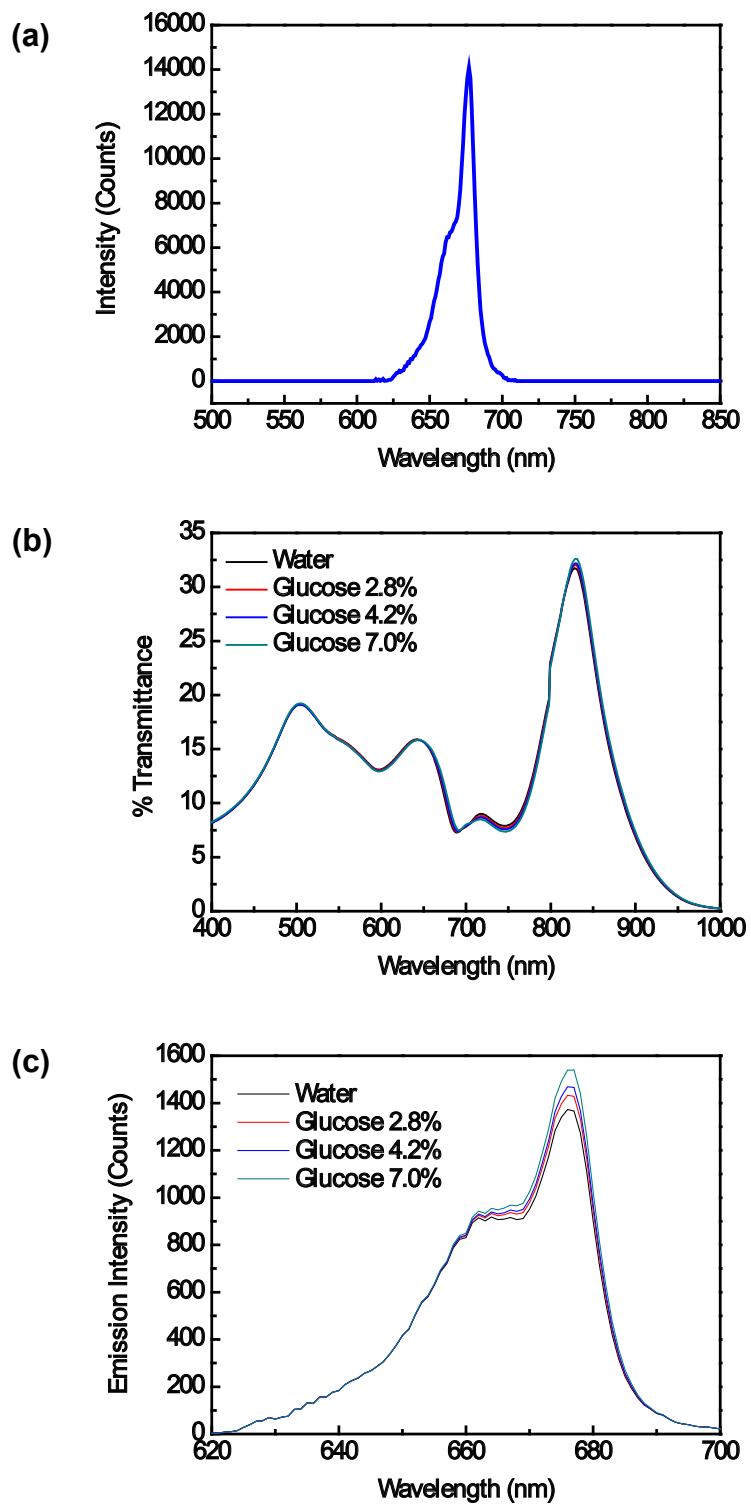


Figure S18

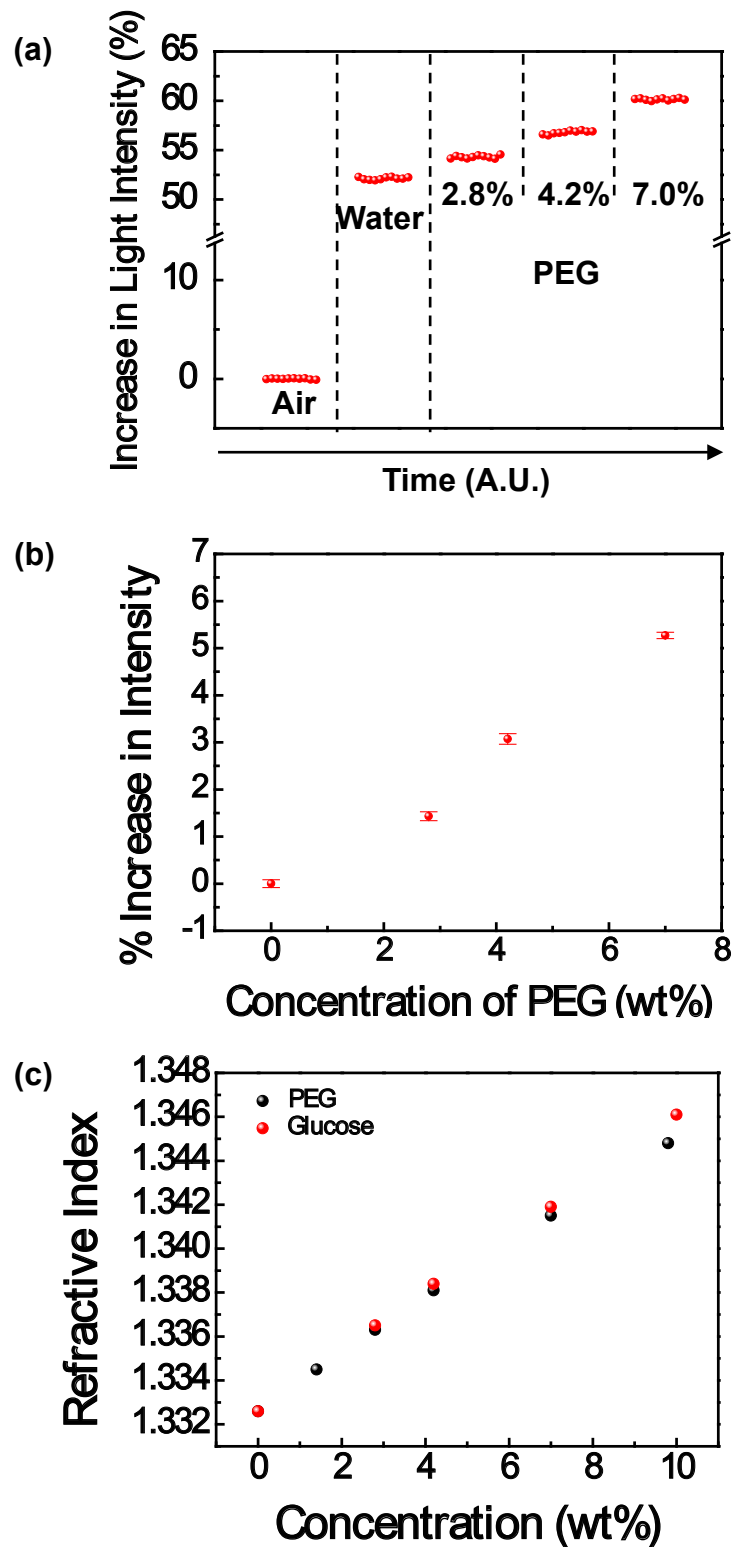


Figure S19

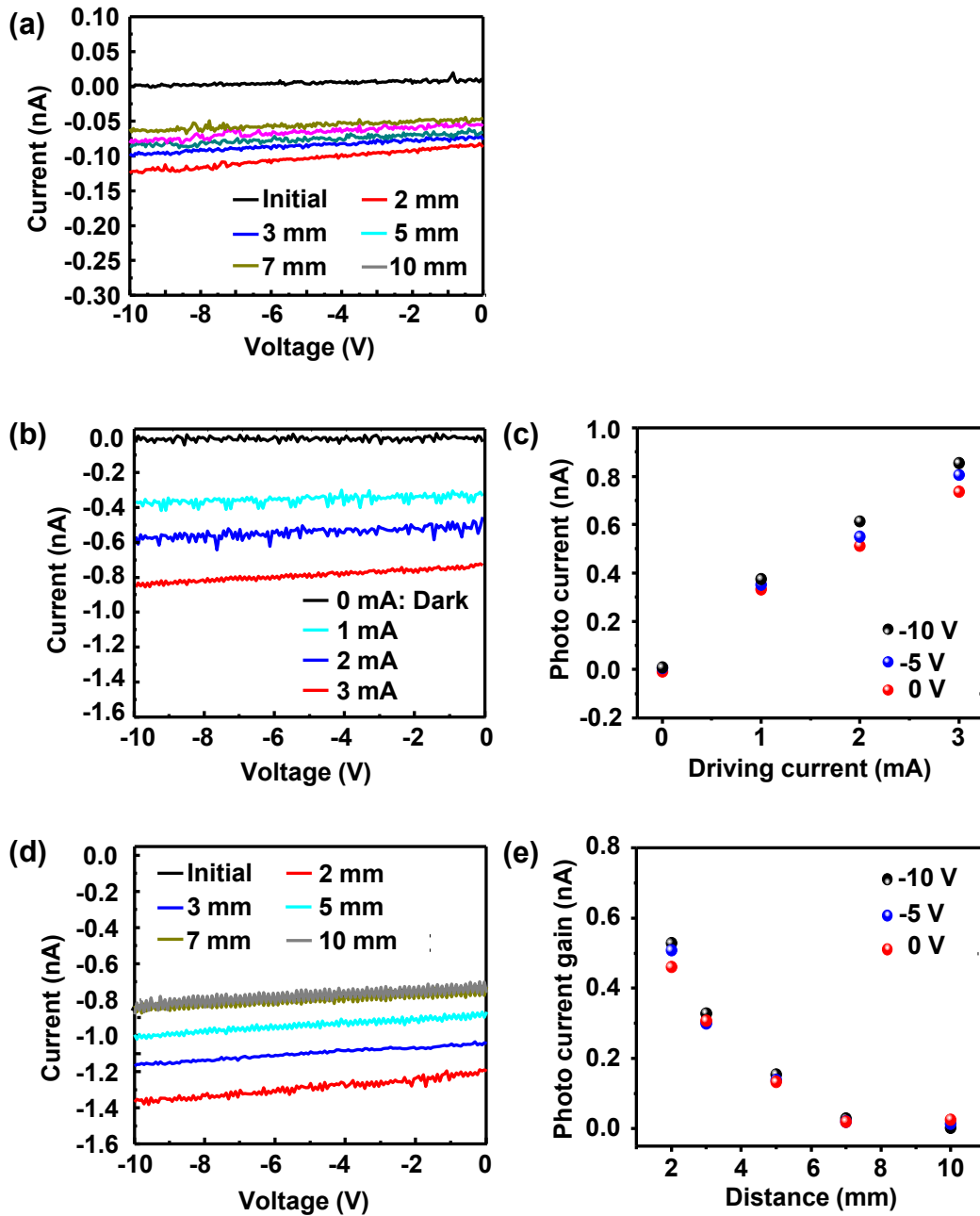


Figure S20

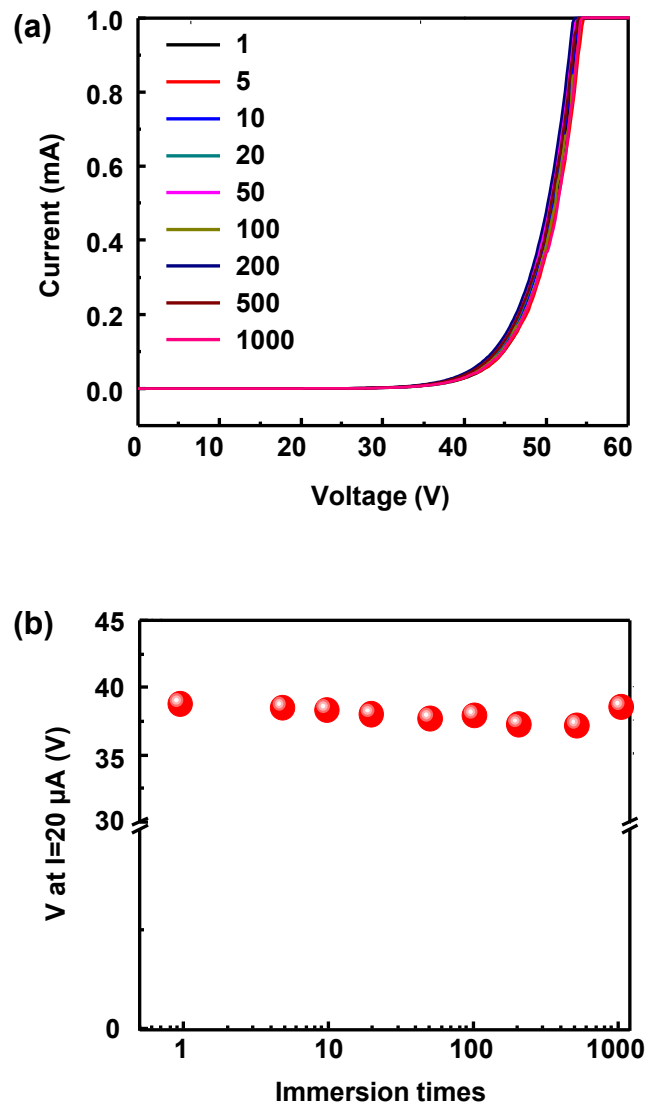


Figure S21

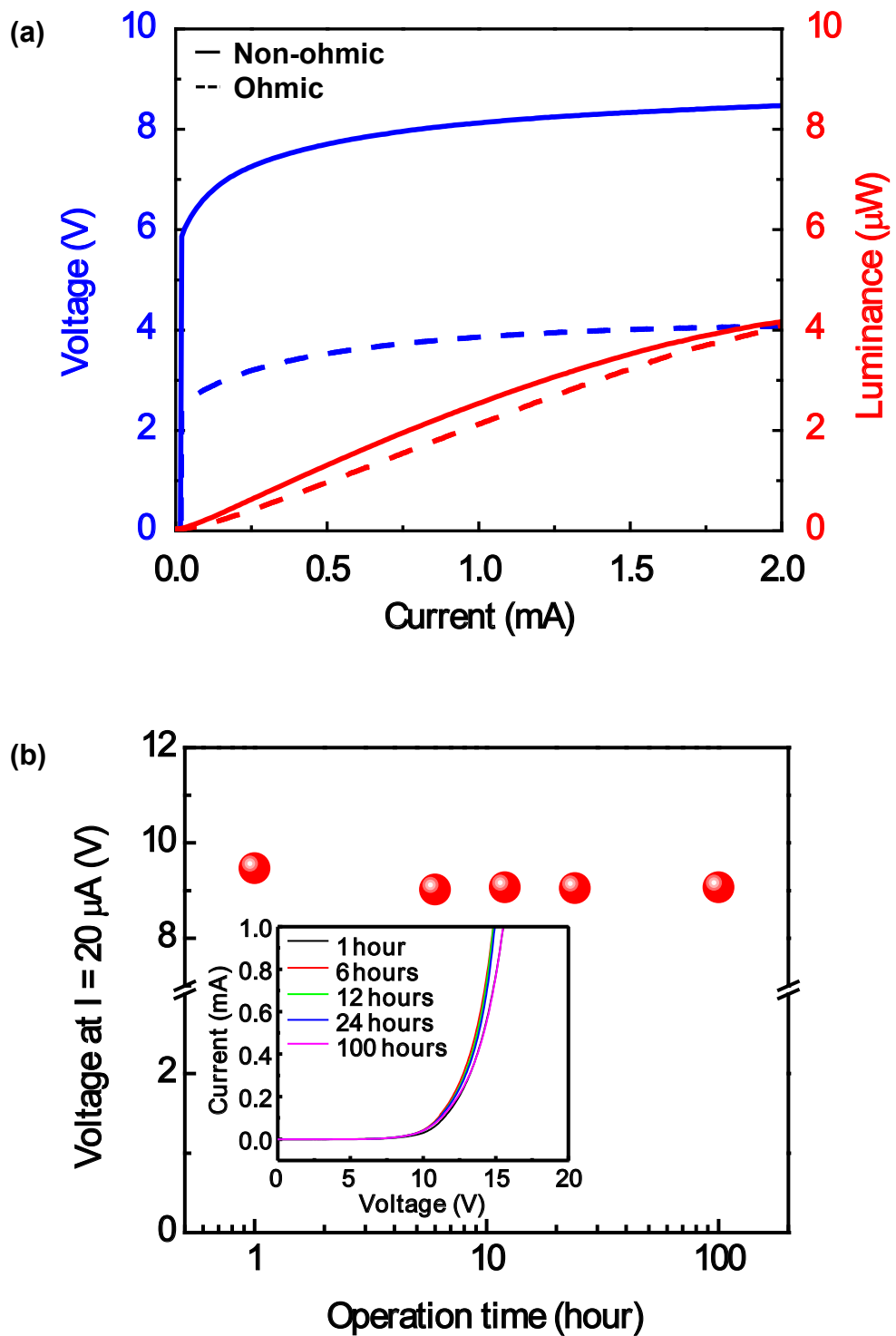


Figure S22

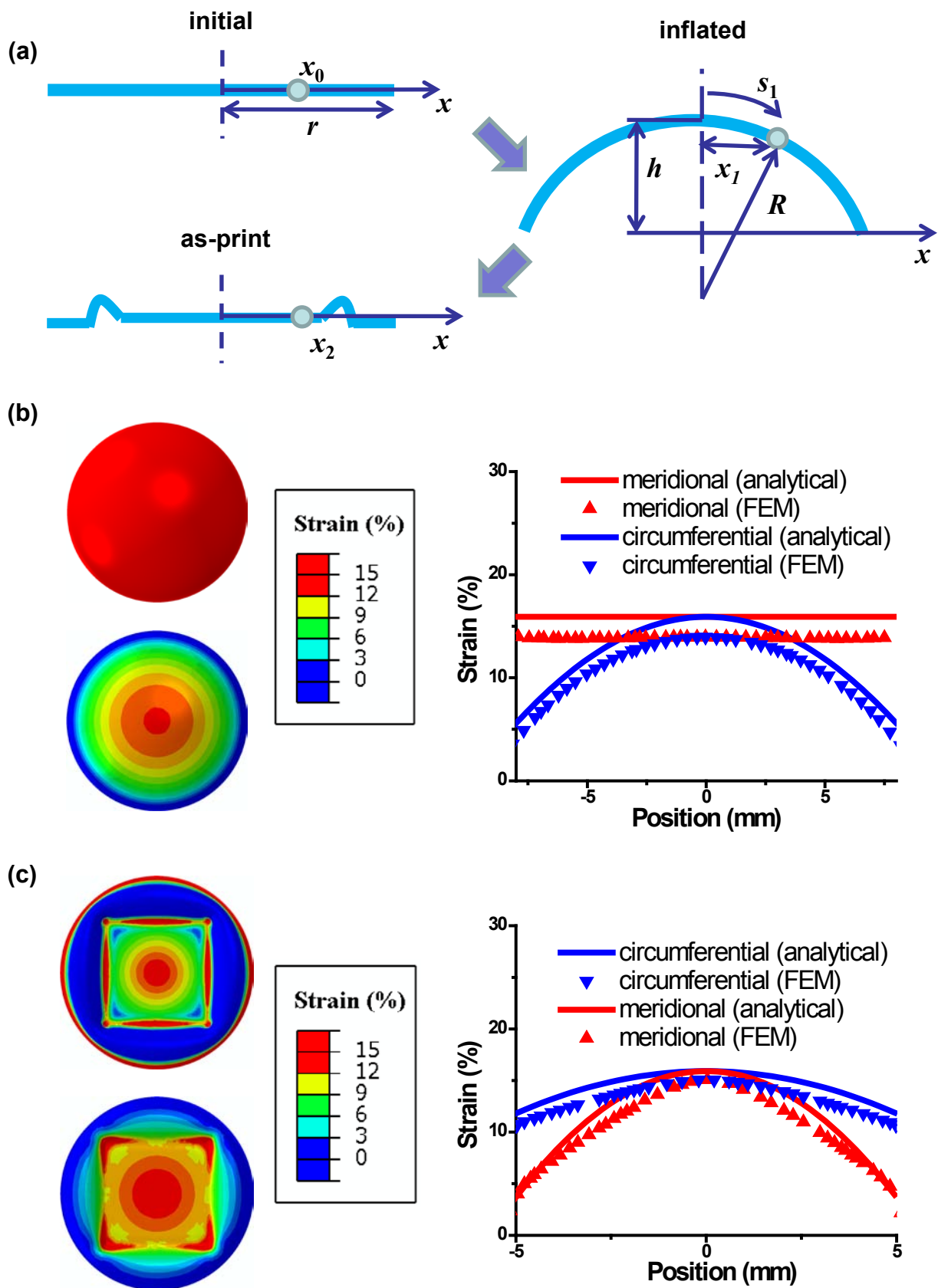


Figure S23

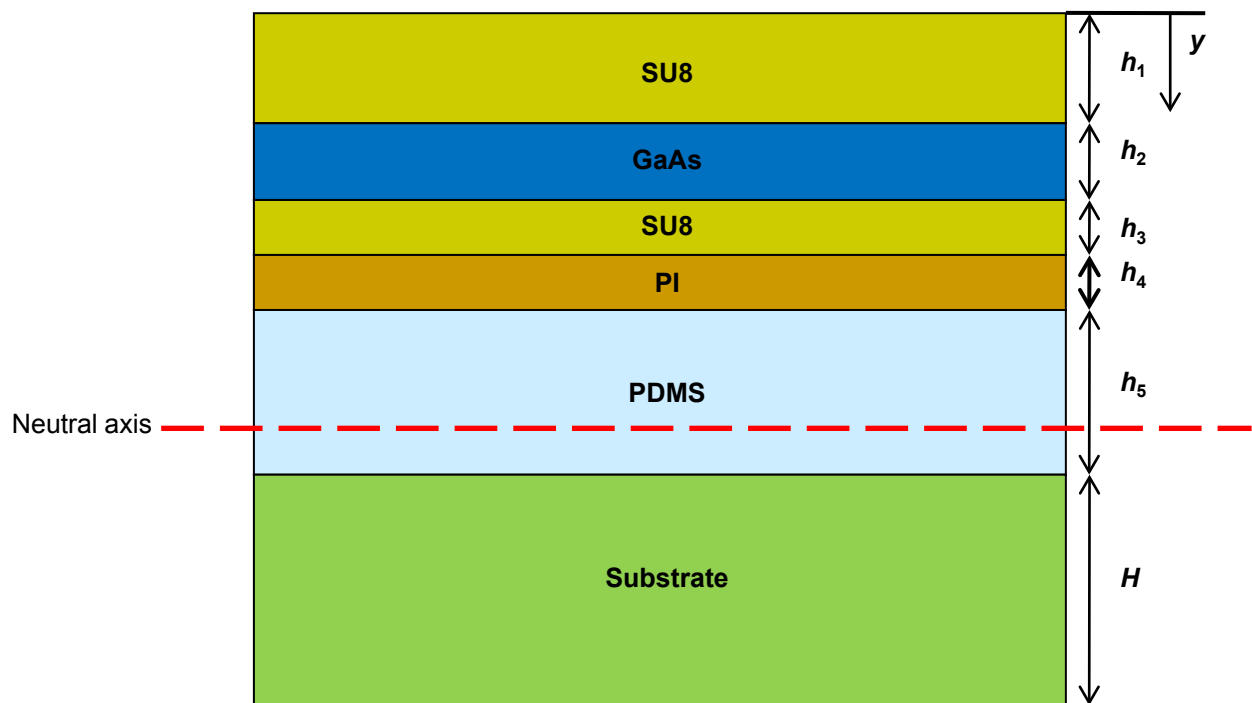


Figure S24